AD-A204 633

REPORT DOCUMENTATION PAGE

Form Approved OMB No. 0704-0188

1a REPORT SECURITY CLASSIFICATION: Unclassified	1b RESTRICTIVE MARKINGS: DTIC FILE COPY
2a SECURITY CLASSIFICATION AUTHORITY	3 DISTRIBUTION/AVAILABILITY OF REPORT: Approved for public release; distribution is unlimited
2b DECLASSIFICATION/DOWNGRADING SCHEDULE	
4 PERFORMING ORGANIZATION REPORT NUMBER(S)	5 MONITORING ORGANIZATION REPORT NUMBER(S): AFOSR-TR- 89-0130
6a NAME OF PERFORMING ORGANIZATION: TRW S&TG; 6b OFFICE SYMBOL (If applicable)	7a NAME OF MONITORING ORGANIZATION: AFOSR/NA
6c ADDRESS (City, State, and ZIP Code): One Space Park, Redondo Beach, CA 90278	7b ADDRESS (City, State, and ZIP Code): Building 410, Bolling AFB DC 20332-6448
8a NAME OF FUNDING/SPONSORING ORGANIZATION: AFOSR/NA; 8b OFFICE SYMBOL (If applicable): NA	9 PROCUREMENT INSTRUMENT IDENTIFICATION NUMBER: F49620-87-C-0059
8c ADDRESS (City, State, and ZIP Code): Building 410, Bolling AFB DC 20332-6448	10 SOURCE OF FUNDING NUMBERS: PROGRAM ELEMENT NO. 61102F; PROJECT NO. 2308; TASK NO. A1; WORK UNIT ACCESSION NO.

11 TITLE (Include Security Classification)
(U) Pulsed Inductive Thruster (PIT) Clamped Discharge Evaluation (Unclassified)

12 PERSONAL AUTHOR(S)
L. Dailey and R. H. Lovberg

13a TYPE OF REPORT	13b TIME COVERED	14 DATE OF REPORT (Year, Month, Day)	15 PAGE COUNT
Final	FROM 6/1/87 TO 12/31/88	31 December 1988	37

16 SUPPLEMENTARY NOTATION

17 COSATI CODES		
FIELD	GROUP	SUB-GROUP

18 SUBJECT TERMS (Continue on reverse if necessary and identify by block number)
Pulsed Inductive Thruster
Electric Propulsion
Plasma Breakdown

DTIC ELECTE S 1 FEB 1989 E

19 ABSTRACT (Continue on reverse if necessary and identify by block number)

The Pulsed Inductive Thruster (PIT) produces the plasma current inductively rather than by an electrode discharge. This research program has addressed the conditions necessary for early plasma breakdown and rapid formation of a diamagnetic current sheet.

While fairly good efficiency has been achieved with a ringing discharge, attempts to improve performance with a clamped discharge have not been successful.

This report presents an analysis of plasma probe measurements of magnetic and electric fields and current sheet density for both ringing and clamped discharge operation, together with development of a numerical model of the current sheet formation which agreed well with the probe data. The cause of poor current sheet formation in the clamped mode has been identified as excessive parasitic inductance. A necessary condition for complete ionization, as well as efficient acceleration, is that the curcuit parasitic inductance be very small relative to the stroke inductance of the thruster coil.

20 DISTRIBUTION/AVAILABILITY OF ABSTRACT	21 ABSTRACT SECURITY CLASSIFICATION
☐ UNCLASSIFIED/UNLIMITED ☒ SAME AS RPT. ☑ DTIC USERS	Unclassified
22a NAME OF RESPONSIBLE INDIVIDUAL: Dr Mitat Birkan	22b TELEPHONE (Include Area Code): (202) 767-4937; 22c OFFICE SYMBOL: AFOSR/NA

DD Form 1473, JUN 86 — Previous editions are obsolete. — SECURITY CLASSIFICATION OF THIS PAGE: Unclassified

Pulsed Inductive Thruster (PIT) Clamped Discharge Evaluation

Contract No. F49620-87-C-0059

TRW Applied Technology Division
Space & Technology Group
One Space Park
Redondo Beach, CA 90278

Final Report

December 31, 1988

Prepared for
Air Force Office of Scientific Research
Bolling Air Force Base, D.C. 20332-6448

Plasma Current Sheet Development in a Clamped Discharge Thruster

C.L. Dailey and R.H. Lovberg

1 Introduction

This report was prepared by the Propulsion and Power Laboratory of TRW's Applied Technology Division. It describes work performed for the Air Force Office of Scientific Research under Contract No. F49620-87-C-0059, to investigate the ionization and current sheet development in an initially un-preionized gas and to evaluate the effect of clamped discharge operation on thruster efficiency.

The Pulsed Inductive Thruster (PIT) used in this investigation produces the plasma current inductively rather than by an electrode discharge. It has been investigated previously [1] as a candidate for Electric Orbit Transfer Vehicle (EOTV) propulsion. In the course of technology development, supported by the Air Force Astronautics Laboratory, the question arose whether a clamped discharge would be more efficient than the ringing discharge mode that had been used for all of the prior work. Surprisingly, the result was an unconvincingly firm negative. One of the changes made in converting the thruster for clamped discharge operation was to mount it coaxially with the vacuum chamber with a relatively small separation between the coil and the chamber wall. Theoretical calculations of the wall interference effect indicated that this could have accounted for the poor performance. To eliminate this possibility, the one meter diameter thruster coil was replaced by a 67 cm. coil for the present study. This also resulted in a 50% increase in the azimuthal electric field, which increased the range available for the present research.

The results of the experimental work, and theoretical modeling performed in order to help understand these results, are presented in this report.

2 Summary

A new thruster, designated MkIV, has been constructed and tested. It is characterized by 1) a smaller diameter coil than its predecessors, i.e., 67 cm, as compared to 1 meter, and 2) a provision for diode clamps in its capacitor bank, which prevent reversal of the driving current, and thereby result in much increased capacitor life. Measurements of I_{sp} and efficiency have been made on an impulse balance, for both clamped and unclamped operation,

and a detailed survey of the electromagnetic field structure and plasma properties in the accelerating region has been made for the unclamped mode.

Thrust balance measurements showed the efficiency of this thruster to be significantly lower than MkI, and no better than MkIII. Unclamped (ringing-mode) operation was significantly more efficient than the clamped mode.

Probe measurements of the electric and magnetic field and current density distributions allowed a determination of the ionization level of the plasma, and inference of the efficiency of the induced plasma current layer as an accelerating piston. It was found that the MkIV propellant was very weakly ionized, and only partially accelerated by the first current sheet. This is in contradistinction to MkI, which displayed tight current sheets, and complete ionization.

A numerical simulation of the plasma breakdown and current sheet formation process allowed a comparison between the MkI and MkIV thrusters, based on such parametric differences as operating voltage, propellant density, and parasitic circuit inductance. It was found possible to achieve quite good agreement between predictions of the code and observed behavior of the two thrusters. It could be concluded that the inefficiency of MkIV was due almost entirely to its parasitic inductance being too high. The effect is that if the current rise rate is not sufficiently high, electron temperature is kept depressed by radiation, and the ionization rate, exponentially dependent on temperature, is too low to provide a highly ionized plasma in the time of the current rise.

This deficiency in the design of MkIV is an easily correctible one; redesign of the connecting and switching circuitry, as well as the use of multiple parallel low-inductance capacitors should bring the relative parasitic inductance of the system to a value below that of MkI.

3 Background

The Pulsed Inductive Thruster is one of three electric thrusters, capable of performing federal and military spacecraft missions, that use electric or magnetic forces to accelerate the propellant. The others are the Ion Engine and the MPD engine, the coaxial counterpart of the inductive thruster which operates in the steady mode.

The PIT is inherently a pulse mode device. It differs from other (non-thermal) thrusters in that it has no electrodes, and from other inductive accelerators in the use of a flat, spiral coil that forces constant radial current density in the coil. While prior technology work showed the PIT to be capable of achieving efficiencies high enough for practical applications, the poor efficiency attained during clamped-mode experiments showed also that the conditions necessary to achieve high efficiency were not well understood.

The 1 m diameter ringing mode thruster, MkI, used for the first thrust balance investigations, gave the highest efficiency and by far the most highly diamagnetic plasma current

sheets of any device tested [1]. This thruster was not operated in the clamped mode. A revised version of this first thruster (MkIII) was tested in the clamped mode, but not in the ringing mode. Its efficiency was found to be far inferior to that of MkI. It was concluded, however, that the clamping itself was not responsible for the change, since during the first quarter-cycle of current, when most of the momentum transfer takes place, the clamping elements had not gone into conduction.

The present program is a continuation of this work, in which a new coil, designed to improve the strength of the ionizing electric field, was incorporated into the thruster. A more extensive diagnostic and analytical effort has been undertaken, in an effort to better understand the underlying physics of the plasma formation and acceleration process, and thereby to have a better basis for efficient thruster design.

3.1 Advantages of the Concept

Freedom from electrode erosion, a unique feature of this thruster, ensures very low spacecraft contamination and makes it possible to design a thruster of unlimited life. Because of the large coil size relative to the MPD thruster, its radiant power loading is significantly less; and because of its small thruster area relative to the Ion Engine it is capable of handling more power for a given engine size. Consequently, it is a natural choice for a high power EOTV. The pulse mode of this thruster makes it well suited for missions requiring fine impulse bit control, and for applications to spinning satellites in which the impulse bits must be sychronized with the rotation.

Another advantage of pulsed mode operation is that the performance of the thruster is characterized completely by the properties of a single pulse. Thrust at a given I_{sp} can be varied from an arbitrarily small value to the maximum available for a given power by simply increasing the pulse rate. Pulsed mode capability is also a great advantage in experimental work. The sensitivity to background pressure, that plagues D.C. thrusters, is entirely absent for the inductive thruster which produces its characteristic impulse bit before gas returning from the wall has had time to reenter the discharge. In this way, the thruster operates in an effectively perfect vacuum, even with slow facility pumping speed.

3.2 Problems of the Concept

3.2.1 Propellant Injection

Proper placement of the injected gas is difficult to achieve. For high efficiency, the gas layer must be located close to the coil, and a high fraction of the gas injected must be in that closely coupled layer. Work done to date in this area has been adequate to permit studies of ionization and current sheet buildup, and thrust balance measurement of I_{sp} and efficiency, but for a practical thruster more effort will be required to improve the radial uniformity and tightness of coupling between the mass layer and the coil.

3.2.2 Propellant Valve

The gas injection valve is a magnetically driven, mechanical device that must operate in a fraction of a millisecond for an essentially unlimited cycle life. In the earlier program [1] a life of a few million shots was demonstrated with a valve design that used a thin, stainless steel diaphragm brazed to a cylindrical, alumina coil form. Repeated failures were encountered due to fatigue cracks associated with stress concentrations induced by the brazing procedure. A different method of attachment is needed that does not rely on brazing.

3.2.3 Switching

Experience with the 1-meter diameter, ringing discharge thruster has shown that a highly diamagnetic current sheet can be ionized and built up in a time small compared to the current rise time of the first half-cycle. However, it is essential that the current rise time must not be limited by the characteristic time of the switch. In this regard, the spark gap is ideally suited for laboratory work. Its switching time is very short and single shot operation is entirely satisfactory. Conceivably, spark gap switching might be feasible for a practical thruster; but a potentially more attractive concept is an assembly of solid state switches known as Reverse Biased Diode Thyristors (RBDT). No work toward developing a solid state thruster switch has been done as yet.

3.2.4 Energy Discharge Capacitors

This has been regarded as a difficult technology area in the past. However, current state of the art capacitors are now capable of virtually unlimited discharge life at an energy storage density of 15 joules per pound. Test screening at several million discharges is effective in improving lifetime reproducibility.

3.2.5 Thruster Mass

For high power mission applications, the power related mass of an EOTV is dominated by that of the power source. The combined mass of thruster and power processor is about the same for the three high I_{sp} electric thruster candidates.

4 Experimental and Theoretical Background

4.1 Experiments

For several years, TRW has conducted experiments with pulsed inductive accelerator coils ranging in diameter from 0.1 m to 1.0 m. The earliest work, supported by AFOSR,

used static fill gas loading with coil diameters of 0.1, 0.15, 0.2, and 0.25 m. Diagnostics consisted of miniature plasma probes (magnetic and electric fields and current density). Subsequent work, supported by AFRPL, used larger coils 0.3 and 1.0 m in diameter and thrust balance data in addition to the plasma probe measurements. Both static fill and pulsed injection gas loading were used with these coils, the latter being necessary for the thrust balance measurements. In all of this work, the accelerator circuit consisted of the coil, an energy discharge capacitor bank, and a spark gap switch. In every case, regardless of thruster size, a highly diamagnetic current sheet formed in the un-preionized gas in about 200 nanoseconds, a time small compared to the 2 microsecond current rise time of the accelerator.

The reason for going to coils of larger diameter was that the efficiency was observed to increase dramatically as the diameter increased. Efficiency was practically undetectable for the 0.1 and 0.15 m diameter coils. For the larger coils it was still very low but rapidly improving with increasing diameter. The results were:

Diameter	I_{sp}	η
0.2 m	1200 s	0.05
0.3 m	1470 s	0.18

Table 1: I_{sp} and efficiency for two thrusters.

A theoretical model, anchored to these data, was developed to indicate the efficiency improvement that might be expected by increasing the diameter to 1.0 m, the largest size that seemed reasonable for the available 1.22 m vacuum chamber. The promising results of this analysis [1] led to the construction of two 1.0 m diameter coils, one of copper tubing supported by TRW, the other of a multistrand flat ribbon similar to Litz wire supported by AFRPL. Thrust data were measured only for the latter coil.

5 Thruster Parameters

5.1 Coil

As mentioned earlier, the present thruster coil is similar to all of the previous pulsed inductive accelerator coils. It differs only in diameter which is 67 cm. The smaller diameter, compared to the 1 m coil, provides a greater azimuthal electric field for a given capacitor voltage and eliminates the possibility of inductive coupling with the 1.22 m diameter vacuum chamber wall. The coil consists of 24 one turn spirals separated 15 degrees from each other and connected in parallel. Current is returned through radial conductors on the back side, separated 1 mm from the spirals. The resulting current density in the coil is purely azimuthal and constant everywhere except over the outer 4 cm radius where the

strands are more closely spaced to increase the local radial magnetic field. This technique was used with the previous 1 m coil to compensate for the loss of magnetic pressure that would normally occur at the coil edge due to field fringing.

The coil strands are placed in grooves machined in plastic plates and the sandwich impregnated with epoxy. This leaves the coils separated 1 mm from the plasma. Additional insulation is provided by a 3 mm thick sheet of glass. The resulting 4 mm separation between the coil and the plasma represents a parasitic inductance that is small, but not negligible, compared to the vacuum coil inductance of about 520 nh. While this separation is much smaller than the 8 cm decoupling distance of this coil, it has a noticeable effect because of the high magnetic field near the face of the coil.

The spark gap configuration of this thruster is also different from that of the 1 m thruster. It uses axial rather than radial current return conductors that result in greater parasitic inductance. Other differences contributing to more parasitic inductance are the use of fewer capacitors and a smaller number of coil strands. The addition of diode clamps inside the capacitors, as described below, also added some parasitic inductance.

5.2 Capacitor Bank

The capacitors used for the present program were taken from the earlier 1 m thruster program. The original 1 m thruster, Mark I, had a single spark gap and four 5 μF capacitors for a total bank of 20 μF. The second version, Mark II, used 12 smaller capacitors for the same capacitance, each with its own spark gap. Toward the end of the previous program, 12 of these capacitors were modified for clamped discharge operation by removing some of the pads to make room for the string of diodes used for the clamp. This reduced the capacitance of each unit to 1.34 μF. The individual spark gaps were removed and the 12 capacitors discharged in parallel through the single spark gap that had been used with the Mark I thruster.

This modified version of the original 1 m thruster, Mark III, was tested at the end of that program. A few thrust balance tests were run up to 20 kV before diode failures occured in two of the units. This was the first indication of very poor efficiency associated with clamped operation. It was also the only thrust balance data obtained with the Mark III thruster. Consequently, the Mark I data represents the only thrust balance data in the ringing mode for any 1 m thruster. This leaves open the possibility that the poor performance of the clamped Mark III thruster may not have been due to the clamped mode, but possibly to some change in the thruster configuration that was the same for both the Mark III 1 m thruster and the present 67 cm thruster, MkIV. This possibility is discussed further below.

Tests were run, in the current program, using the 10 remaining 1.34 μF clamped capacitors at voltages up to 18 kV, while 6 additional units were being reworked with higher voltage diodes capable of operating up to 25 kV. These high voltage clamps were physi-

cally larger than the original ones, requiring further reduction of the capacitance to 0.97 μF each. Because of the high cost of the diodes, only 6 capacitors were modified for 25 kV clamped operation. After testing this configuration up to 24 kV, again with very poor efficiency, two further capacitor changes were made. One consisted of disconnecting the diodes in the ten clamped capacitors, and adding two of the original nominal 1.67μF units and operating the MkIV thruster in the ringing mode with a measured capacitance of 17.4μF.

The other change was to replace the pads of the 6 high voltage clamped units with much higher capacitance pads. By going to a lower voltage, all film pad design, the capacitance of each unit was increased to 4.5 μF. Because of a failure of one of the series sections in one of these capacitors during acceptance testing, its capacitance increased to 6.2 μF, giving a total bank of 28.7 μF. This large change in capacitance made little difference to the measured thruster efficiency.

5.3 Propellant Increment

The propellant mass (argon) injected per shot ranged from 1 to 10 milligrams. The propellant injection valve and method of measuring total mass and mass distribution, both radially and axially in front of the coil, are described in detail in Ref.[1] . Several changes were made to the gas injection nozzle to improve the distribution over the smaller coil. The final results are shown in Figure 1.

6 Thrust Balance Performance Data

Figure 2 compares thrust balance measurements of thruster efficiency and I_{sp} for the 1 m and 67 cm thrusters in the ringing discharge mode, and the smaller thruster in the clamped mode for three different values of capacitance. The two conclusions to be drawn from these data are that the clamped mode is much less efficient than the ringing mode for the smaller thruster, and that the ringing mode for the smaller thruster is much less efficient than the same mode for the larger thruster.

These data represent the total thrust balance data base for the 1 m and 0.67 m thrusters. Further insight into their performance, obtained from an analysis of probe data and the theoretical model, is described later.

7 Probe Mapping

Distributions of magnetic field (B_r), current density (J_θ), and axial electric field (E_z) were measured by means of appropriate probes. The magnetic probe was a 2 mm diameter solenoid, encased in a 6 mm glass jacket, and mounted on a two-axis carriage that allowed scanning over that portion of the $r - z$ plane in which acceleration takes place. Data were

recorded over a grid of 60 points, 12 points in z at each of 5 evenly spaced radii. Z stations were spaced at 5 mm intervals within 3 cm of the coil face, and at 1 cm intervals farther downstream. Current density was measured with a miniature Rogowski coil scanned over the same spatial grid.

The B_r probe was calibrated by direct comparison of its output with that of an accurately formed 1 cm^2 standard placed in the same pulsed test field. Such a procedure was not possible for the Rogowski coil, however, since its sensitivity includes its effective window area as a factor; this area will generally be somewhat different from the geometrical area of its opening. Rather, it was calibrated against an axial B_r gradient measured in the pulsed plasma at a position near the coil and near its mid-radius, where the $\partial B_z/\partial r$ contribution to J_θ is negligible. The outputs of both probes were integrated by a passive R-C integrator of 120 μs time constant.

The axial electric space-charge field was measured with a differential electric probe. The probe electrodes themselves were 5 mm lengths of #16 copper wire, aligned along r, and separated along z by 6.5 mm. They were connected to the primary winding of a carefully shielded ferrite-core pulse transformer whose function is to cancel all "common-mode" components and leave only the differential signal.

All probe data were recorded by a digital transient recorder of 8-bit resolution and 20 MHz sampling rate. Records were archived on magnetic disk media.

8 Results; Comparison with MkI

This section presents distributions of the density and electromagnetic field quantities obtained from the MkIV thruster. Since, as has been mentioned, the efficiency of this thruster has been found to be markedly inferior to the 1-meter MkI thruster, data from that device are included in order to attempt an explanation of the difference.

For these diagnostic runs, the bank (17.4 μF) was operated without diode clamping. This provides a twofold advantage. First, the dynamics of the second and third half-cycle plasma currents provide an indication of the amount of gas left behind by the first current sheet (where, in clamped operation, the first sheet would have to accelerate the entire gas fill); secondly, an informative comparison can be made with the performance of the unclamped MkI thruster, which was reasonably efficient.

The data shown here were for 20 kV on the bank, and an injected propellant mass of 3.6×10^{-5} kg of argon. Since the physics of the coupling between fields and propellant was the subject of this run, data were taken only at a radius of 25 cm (near the mid-radius of the coil), where the z-dependence of the measured parameters could be assumed to be typical of the coil face as a whole.

8.1 B Field Distribution

A superposition of $B_r(t)$ traces, taken at axial positions z=1,..,6 cm, is shown in Figure 3. It is seen first that all the traces begin to rise immediately at t=0; this is indicative of rapid early diffusion of the field through the plasma, which in turn indicates poor early conductivity. The negative swing of the traces, which begins at z=1 cm at about 8 μs, is by contrast a discretely ordered series of rises, indicative of a current sheet propagating outward at a velocity of about 1.6 cm/μs. With the magnetic pressure difference indicated in the figure, this implies an average plasma density encountered by the second current sheet over the 1-6 cm range of about $5 \times 10^{20} m^{-3}$, which corresponds to approximately 20 μ of the original fill pressure of approximately 600μ.

By contrast, a corresponding set of $B_r(t)$ traces from MkI (Figure 4) show less initial diffusion, and a better formed first current sheet. Subsequent to the passage of the current, the traces have nearly identical time behavior, indicating that the spatial field distribution in the 1-6 cm zone is approximately flat; this can only occur if negligible plasma is left behind by the current sheet.

In Figures 5 and 6, $B_r(z)$ is shown at five times for the two thrusters. Here, it is also evident that diffusion of the accelerating B field through the plasma is much more pronounced in MkIV than in MkI.

The different behavior of MkIV and MkI during the second current half-cycle is evident from Figures 7 and 8. In the 8-11 μs time interval, the MkIV $B_r(z)$ distributions exhibit a strong positive slope, indicative of substantial mass loading, while $B_r(z)$ for MkI remains nearly flat as it swings from positive to negative values.

8.2 Azimuthal E Field

A premise in the original design of the MkIV coil was that its reduced diameter (67 cm, as compared to 100 cm for MkI) would *increase* E_θ by: 1) decreasing the circumferential distance over which the terminal voltage would be applied, and 2) increasing radial spacing between the coil and the vacuum tank wall, so that the effect of the wall as a shorted secondary turn near the coil would be reduced.

However,the magnetic probe data shown in the previous section are suggestive of an actual deficiency in E_θ in MkIV, since early conductivity seems lower than in MkI. This hypothesis can be tested by an integration of B_r over z and differencing such integrals at adjacent timesteps in the data.

The flux of B_r per unit circumference is

$$\Phi = \sum_{i=1}^{n} B_r(z_i)\Delta z_i \qquad (1)$$

where n is the number of z points in the B probe scan. Then,

$$E_\theta = \frac{\Delta\Phi}{\Delta t} \tag{2}$$

This is an expression of Faraday's law that holds irrespective of the ratio of diffusion to convection of the field in the plasma.

The results of these computations are shown in Figures 9 and 10[1]. It can be seen that for MkIV, the initial E_θ is approximately 1 kilovolt/meter, an unusually low value for initiation of a pulsed discharge. The corresponding initial E_θ for MkI is between 2 and 3 kv/m, the larger coil diameter notwithstanding. In each of these curves, the subsequent rise of E_θ up until 2 or 3 μs is due to the addition of a $\mathbf{v} \times \mathbf{B}$ term as the plasma accelerates away from the coil.

8.3 Plasma Density

If separate equations of motion for the ions and electrons in a plasma are written and combined, under the assumption of quasi-neutrality and scalar pressure, as well as the negligibility of certain terms that depend upon the electron-ion mass ratio, there is obtained, upon addition of the two equations, the MHD equation of motion for the plasma as a whole, and upon subtraction, a relation known as the generalized Ohm's law. The derivation is carried out in Spitzer's classic monograph, for example[2].

A form of Ohm's law appropriate for these experiments is

$$\mathbf{E} + \mathbf{v} \times \mathbf{B} - (1/n_e e)\left[\mathbf{J} \times \mathbf{B} - \nabla p_e\right] - \eta \mathbf{J} = 0 \tag{3}$$

where

$$\begin{aligned} \mathbf{v} &= (m_e \mathbf{v}_e + m_i \mathbf{v}_i)/(m_e + m_i) \\ p_e &= nkT_e \\ \eta &= m_e/n_e e^2 \tau_e \end{aligned}$$

where τ_e is the mean collision time of electrons with ions or neutrals.

Since, in the PIT, $\mathbf{v}$ is purely axial (along z) and $\mathbf{J}$ is along θ, the z-component of Ohm's law becomes

$$E_z - \frac{1}{n_e e}\left[J_\theta B_r - \frac{\partial p_e}{\partial z}\right] = 0 \tag{4}$$

In the event that the $\mathbf{J} \times \mathbf{B}$ force term is dominant over ∇p_e, this reduces to

$$E_z \simeq \frac{J_\theta B_r}{n_e e}$$

[1]The large noise at early times in these results is due to the differencing of adjacent time values of B, which, for the first microsecond or so is itself a noisy signal.

which then enables a determination of the electron density distribution through the experimentally measured distributions of B_r, J_θ, and E_z:

$$n_e = \frac{J_\theta B_r}{eE_z} \tag{5}$$

Previous experiments employing these combined probe analyses have usually had a domi nt Lorentz force; Equation (5) has proved adequate to produce electron density distributions that have agreed well with optical refractivity measurements of the same plasma [3].

Two relational criteria must be met by B_r, J_θ, and E_z in order for Equation (5) to be valid: First, since E_z is in the denominator, its passage through a value of zero must be accompanied by a simultaneous passage of one of the numerator factors through zero; otherwise an infinite density would be implied. Secondly, the numerator ($J_\theta B_r$) and the denominator (E_z) must always have the same sign, since density is always positive.

Figure 11 is a superposition of raw data traces of B_r, J_θ, and E_z, taken near the coil face, at z =0.5 cm. The vertical scale corresponds, in each case, to the size of the 8-bit word in the transient recorder. For clarity, E_z is plotted in reverse polarity. It can be seen here that the zero crossings of E_z are nearly simultaneous with crossings of one or the other of the other two traces, especially for times earlier than 10 μs. The stricture on sign agreement is also well obeyed. Figure 12 is a calculation of $n_e(t)$ from these data, using Equation (5). The short transient excursions of n_e below zero at times near 5, 13, and 18 μs are due to the very slight residual zero crossing disagreement. The three distinct peaks in n_e correspond to the formation and subsequent sweeping forward of the three successive current sheets. Their relative heights are indicative of the fraction of the original propellant fill left behind by the first current sheet.

Figures 13 and 14 are a similar set taken at z=1.0 cm. The peaks in n_e are narrower and higher than in the previous set because the plasma sheets have been made denser through snowplowing of plasma between the two stations, and have acquired a forward convective velocity so they are in the probe position for a shorter time. The second plasma sheet is particularly thin and dense because it is compressed between the two opposing B_r fields that the current sheet separates. A sharp dip may be seen in E_z at the time of passage of each of these layers. In the case of the second sheet, the dip is close enough to zero to introduce a large probable error in the value of n_e inferred from it.

In Figures 15 and 16, sets of B_r, J_θ, and E_z are displayed for z=2.0 cm and 3.0 cm. Here, there are serious departures from the criteria for use of Equation (5) for reduction of the data. In the 2 cm case, for example, E_z reverses sign near 3 μs and 11 μs, where no corresponding crossing of either B_r or J_θ occurs. The sharp oscillatory character of the fluctuation in E_z that carries it through zero makes it clear that the electron pressure gradient term must be included. If a sheet of significant electron pressure moves forward in z past the probe, the signal should first swing negative and then positive as the density

peak passes. The clearest instance of this occurs in Figure 15 near 20 μs; the effect is present in the E_z trace near 4 and 10 μs as well, but is obsured by the dip in E_z due to the peak in n_e.

The presence of a significant electron pressure gradient effect makes it impossible to infer density with the present probe data alone. Such an inference would be possible under the assumption of an isothermal plasma, in which case Equation (4) would become, for each spatial point, a differential equation in $n_e(z)$. The actual solution of the whole set of these would be a cumbersome iterative process, probably not justified in view of the uncertainty of the isothermal assumption.

It has been possible, however, to obtain an informative and significant distribution of $n_e(z,t)$ for early times, specifically during the breakdown phase. This is shown in Figure 17. The most important result here is that the ionization proceeds unusually slowly. Full plasma density is not attained for 2.5 μ-seconds and during this time the discharge current has reached half of its peak value. Plasma resistivity and the associated diffusion of the field are high, and efficiency is accordingly degraded.

9 Simulation of Breakdown Phase

In order to better understand the physics of the breakdown of the neutral gas propellant on the face of the PIT coil, a computational simulation of the problem has been undertaken. This study has been limited in scope to the formation and heating of the plasma, and the diffusion of magnetic flux through it during ionization and current sheet formation.

Any plasma simulation that includes in the maximum detail all the physics that can plausibly be significant in a problem such as this will be massive in terms of the size of the code, computational facilities required, and programmatic effort. A few such codes exist. However, in instances where the area of interest is somewhat restricted, and where physical conditions allow reasonable approximations to some parameters to be made, or others to be neglected, a relatively simple program can supply significant answers.

In the present instance, magnetohydrodynamics has been neglected altogether, under the assumption that plasma motion during the breakdown phase will not affect the process materially. It is assumed that the plasma is transparent to its own radiation, so that radiation transport is not an issue. Close to the coil, over most of its area, spatial dependences of variables are mainly axial (along z), so a one-dimensional calculation is adequate. Other simplifying approximations are discussed in the separate subsections below.

9.1 Computational Grid and Circuit

The one-dimensional grid consists of 50 cells, each 4 mm long, along the z axis, the direction of acceleration. The magnetic field B is defined as directed along y, and the current density

and applied electric field along x. This configuration may be visualized as a parallel-plate channel of unit plate separation (x), infinite width(y), and 20 cm length(z).

Parasitic circuit inductance is provided by extending the acceleration channel toward negative z (where plasma is excluded), and applying a fixed driving voltage at its end.

9.2 Ionization

Ionization is assumed to be due to direct electron impact from the ground state, and also from the first excited state. For the latter process, it can be assumed that excitation from the ground state is the rate-limiting step, and that ionization occurs promptly thereafter. The cross sections for excitation and direct ionization are taken from Druyvesteyn and Penning [4]. Each rises linearly near its threshold (10.8 ev and 15.7 ev, respectively), and since the plasma temperature is expected to be no more than about 3 or 4 ev, only the linear portion of each cross section near its threshold will contribute significantly to the ionization rate.

The total ionization rate due to either process is

$$\mathcal{R} = n_e n_o < \sigma v > \qquad m^{-3}s^{-1}$$

where n_e is total electron density, n_o is density of neutrals, and $< \sigma v >$ is the mean of the product of electron velocity and cross section, taken over the spectrum of electron velocities. In terms of the original neutral density n_a, $n_o = n_a - n_e$.

$< \sigma v >$ may be evaluated by starting with the differential ionization rate:

$$d\mathcal{R} = n_o\, \sigma(E)\, n(E) \left(\frac{E}{2m_e}\right)^{\frac{1}{2}} dE \quad m^{-3}s^{-1}J^{-1}$$

where σ and n are now explicit functions of electron energy E. Electrons are Maxwell-distributed:

$$n(E) = \frac{2}{\pi} \frac{n_e}{(kT)^{\frac{3}{2}}} \sqrt{E}\, e^{-E/kT}$$

so that

$$d\mathcal{R} = \frac{2n_o n_e\, \sigma(E)}{\sqrt{2\pi m_e}(kT)^{\frac{3}{2}}} E\, e^{-E/kT} dE$$

where k is the Boltzmann constant and T is the electron temperature in $^\circ K$.

The linearly rising cross section near a threshold E_0 is

$$\sigma(E) = A(E - E_0)$$

where A is obtained from previously cited experimental data [4]. This finally gives, as the total ionization rate for a process,

$$\mathcal{R} = \frac{2An_o n_e}{\sqrt{2\pi m_e}(kT)^{\frac{3}{2}}} \int_{E_0}^{\infty} E(E - E_0)\, e^{-E/kT} dE$$

which integrates to

$$\mathcal{R} = \frac{2An_o n_e}{\sqrt{2\pi m_e}}(kT)^{\frac{3}{2}}\left(\frac{E_0}{kT}+1\right)e^{-E_0/kT}$$

When direct and excitation-ionization rates are combined, using E_0=15.7 ev and $A_0 = 1.9\times10^{-21}$ m^2/ev (direct ionization) and E_1=10.8 ev and $A_1 = 0.3A_0$ (excitation), as well as the approximation $E_{0,1} >> kT$, the result is

$$\mathcal{R} = 1.0\times10^{-14} n_e n_o \sqrt{T}\, e^{-15.7/T}\left(1+0.20\, e^{4.9/T}\right) \quad m^{-3}s^{-1} \tag{6}$$

where T is expressed in ev.

Possible radiative ionization has been neglected in this initial formulation of the problem. It would be a considerable complication over what has been done here, but could be included in further refinements of the code if results indicate it to be a significant omission.

9.3 Heating and Losses

Plasma heating is due only to resistivity; both electron-ion and electron-neutral resistivity terms are included. Losses are due to radiation and ionization cooling.

9.3.1 Resistivity

Plasma (electron-ion) resistivity has the Spitzer dependence on temperature, with the coulomb factor $\ln\Lambda$ equal to approximately 5:

$$\eta_p = 10^{-3}T^{-\frac{3}{2}} \quad \Omega\text{ -m} \tag{7}$$

Electron-neutral resistivity is calculated using cross-sections from Rosa [5]:

$$\eta_n = 1.7\times10^{-6}\sqrt{T}\, n_o/n_e \quad \Omega\text{-m} \tag{8}$$

9.3.2 Radiation

Radiation losses are calculated using an approximation due to Griem [6], which is that for atoms or ions whose first excited states are not unusually low in energy, the principal radiation loss is through the resonance lines; the total loss is fairly well approximated by doubling the resonance line loss. The resonance lines of both AI and AII have nearly the same energy, which allows the simple approximation that all of the original neutral density is radiating at the same rate. With constants evaluated and T in ev, this power is

$$P_r = 2.0\times10^{-31} n_e n_a\, e^{-11.8/T}/\sqrt{T} \quad w\, m^{-3} \tag{9}$$

Here, the energy of the resonance line, $E_2 = 11.8$ ev, appears in the exponent. n_a appears in this expression to provide the approximation that both the neutrals and ions are radiating the same li. ' energy.

9.3.3 Ionization cooling

It is assumed that each ionization removes from the plasma an energy equal to the ionization potential plus the temperature of the newly equilibrated electron.

9.4 Field Diffusion, Current, and E_x

As noted above, the source voltage is assumed constant during the ionization; for the unit width channel, this is represented by a constant applied electric field E_s. Parasitic inductance between this source and the plasma is represented by an additional length l_p of the channel. These may be converted to actual bank voltage and parasitic inductance by multiplication by $2\pi r$ and $2\pi\mu_0 r l_p$, respectively, where r is the radial position of the plasma on the coil face.

Through Faraday's law, E_s may be equated to the time derivative of the flux in the channel:

$$E_s = \frac{d}{dt}\left[l_p B_1 + \int_0^l B(z)dz\right]$$

where $B_1 = B(z=0)$ is uniform over l_p, the parasitic segment of the channel.

For the discrete computational grid, the flux integral is replaced by a summation over the plasma cells. The equation is then integrated, and a further rearrangement gives an expression for updating B_1:

$$B_1 = \frac{1}{l_p}\left[E_s t - \Delta z \sum_{n=1}^{50} B_n\right] \tag{10}$$

The distribution of B in the plasma is governed by the diffusion equation

$$\frac{\partial B}{\partial t} = \frac{\eta}{\mu_0}\frac{\partial^2 B}{\partial z^2} \tag{11}$$

which, when cast into finite difference form, gives the increment of B in the i th cell, per timestep:

$$\Delta B_i = \frac{\eta}{\mu_0}\left[\frac{B_{i+1} + B_{i-1} - 2B_i}{(\Delta z)^2}\right]\Delta t \tag{12}$$

where $\eta = \eta_p + \eta_n$, the sum of the electron-ion and electron-neutral resistivities.

The current density in each cell is

$$J_i = \frac{1}{\mu_0}\left[\frac{B_{i+1} - B_{i-1}}{2\Delta z}\right] \tag{13}$$

9.5 Computation Algorithm

At each timestep:

- The B_i in the plasma channel are summed to get a new flux integral.
- This integral is differenced with that from the previous timestep and divided by Δt to obtain E_x, the electric field at the coil insulator.
- B_1 is evaluated with Equation (10).

Then, at each cell, and within the particular timestep:

- $\eta(n_0, n_e, T)$ is evaluated through Equations (7) and (8).
- A new array $B1_i = B_i + \Delta B_i$ is evaluated through Equation (12) (diffusion equation) and the new η.
- n_e is updated through Equation (6).
- T_e is updated through the energy balance equation

$$\frac{dT}{dt} = \frac{\eta J^2 - P_r}{e\, n_e} - \mathcal{R}\frac{15.7 + T}{n_e} \tag{14}$$

- The B array is replaced by the $B1$ array, time is advanced, and the cycle repeated.

9.6 Stability of Computation

The diffusion equation (Equation (12)) is made nonlinear by the dependence of η on field quantities, so it might be anticipated that the ordinary stability criteria for the first order explicit integration scheme employed here might not be adequate. This has proven to be the case. For a constant diffusivity (η/μ_0) the timestep requirement for stability is that

$$\Delta t \leq 0.5\frac{\mu_0(\Delta z)^2}{\eta}$$

For these calculations, a timestep limit for stability has been found, but it is approximately ten times smaller than that given above. For the parameters of the computations done here, a timestep of 1.0×10^{-9} sec is adequate.

9.7 Program Inputs: Initial Conditions

The propellant is assumed to be initially deposited against the coil with a distribution decreasing exponentially in z, with a scale thickness of 6 cm. Its peak density is a variable input parameter, and it is 1% ionized at t=0. Its initial temperature is set at 0.1 ev. For the MkI thruster, the peak cold propellant pressure is 100μ, and for MkIV, 600μ[2].

E_s and l_p are also assigned as program inputs. Since the experimental data against which these computations are compared is taken at a radius of 27 cm on MkIV and 40 cm on MkI, $V_0 = 1.7E_s$ on MkIV and $2.5E_s$ on MkI, while the actual parasitic inductance is $L_p = 2.1 \times 10^{-6} l_p$ on MkIV, and $3.1 \times 10^{-6} l_p$ on MkI. L_p may be determined for each thruster from its initial dB/dt or alternatively, from the time of its first current peak, when the principal inductance in the circuit is still the parasitic component. For MkI, this gives $L_p = 130nH$ ($l_p = .04m$), and for MkIV, $L_p = 320nH (l_p = .15m)$.

For both thruster data runs, the bank voltages corresponded to electric source fields E_s of approximately 10000 V/m.

9.8 Results

Since plasma dynamics are not included in these computations, the comparisons made here are restricted to early times. All computations were terminated at a time of 2.0 μs.

For the rates of ionization and radiation given in Equations (6) and (9), Table 2 compares MkI and MkIV data with computations. The parameter f_{ion} is fractional ionization.

	MkI		MkIV	
	calc	exper	calc	exper
$B_r(2\mu s)$	.35	.35	.11	.13
$E_\theta(0)$	2.5×10^3	$2.5 \pm 1 \times 10^3$	1.5×10^3	$1.3 \pm .3 \times 10^3$
f_{ion}	.80	—	.02	$.1 \pm .05$
T_e	3.9 ev	—	2.1 ev	—

Table 2: Calculated and measured parameters for MkI and MkIV thrusters. Ionization rate constant = 1.0×10^{-14}.

Agreement of B_r values at $2\mu s$ and E_θ at $t = 0$ is seen to be excellent; fractional ionization, for which experimental values were only obtained for MkIV, is somewhat low[3].

[2]This pressure, while higher than what would ideally produce I_{sp} in the 1500-2000 second range, was that employed for the complete E, B, and J mapping of Run 25.

[3]Since the computation assumes a constant source voltage, the experimental values given for B_r are those *projected* to $2\mu s$ from the earlier slopes

In order to compensate for the neglect of radiative ionization and ionization from excited states other than the first, the ionization rate constant in Equation (9) was ajusted upward from its original value of 1.0×10^{-14}. Table 3 presents values for an increase of the rate constant by a factor of 20.

	MkI		MkIV	
	calc	exper	calc	exper
$B_r(2\mu s)$	.33	.35	.11	.13
$E_\theta(0)$	2.5×10^3	$2.5 \pm 1 \times 10^3$	1.6×10^3	$1.3 \pm .3 \times 10^3$
f_{ion}	1.00	—	.07	$.1 \pm .05$
T_e	3.9 ev	—	1.5 ev	—

Table 3: Calculated and measured parameters for MkI and MkIV thrusters. Ionization rate constant $= 2.0 \times 10^{-13}$.

Here, there is fairly good agreement between calculated and measured ionization fractions. The MkI ionization for this case is 100%, which is in accord with the observation in that experiment that optical spectra from neutrals were entirely absent.

The different electron temperatures and conductivities displayed by MkI and MkIV result in differing initial current sheet thicknesses. $B_r(z)$ in any case tends toward an exponential ditribution; the clearest display of diffences in diffusion depth is then a semi-log plot for which the slope of the distribution curve is proportional to the current layer thickness.

Figure 18 shows plots of $\log(B_r)$ vs. z for the two thrusters. The current sheet thicknesses are 5.1 cm for MkI, and 9.0 cm for MkIV.

10 Conclusions

- Prior work with the MkI PIT in the ringing discharge mode has demonstrated the feasibility of the concept, with fairly good efficiency in the I_{sp} range of interest for Earth orbit missions.
- While clamped discharge operation is expected to improve thruster efficiency, this has not yet been demonstrated, either with the MkIII or MkIV thrusters.
- The present analysis of MkI and MkIV first quarter-cycle data, together with a numerical model developed to describe initial plasma breakdown (ionization and current sheet formation) has shown the crucial importance of circuit parasitic inductance.

- The large indicated parasitic inductance of MkIV, probably due mostly to internal capacitor inductance associated with diode modifications, is not an essential limitation of the PIT concept, and could readily be brought to a value lower than that of MkI in a new design.

- It has been understood throughout the history of pulsed thruster research that parasitic inductance is detrimental to efficiency, through the theorem that efficiency can never be greater than the fractional increase in inductance during the acceleration stroke. It has been discovered in this work that a more serious consequence of parasitic inductance is its effect on initial plasma breakdown and current sheet formation.

  In fact, the disastrous loss of ionization rate incurred through high parasitic inductance is sufficient to explain the poor current sheet formation and low thrust efficiency of all thrusters since MkI.

References

[1] C.L. Dailey and R.H. Lovberg, "Pulsed Inductive Thruster Technology", AFAL TR-87-012, April 1987.

[2] Lyman Spitzer,Jr. "The Physics of Fully Ionized Gases" Interscience, New York, 1956.

[3] C.L. Dailey and R.H. Lovberg, *AIAA J.* **10**, no.2, 125, 1972.

[4] M.J. Druyvestyn and F.M. Penning, *Rev. Mod. Phys.*, **12**, 87, 1940.

[5] R.J. Rosa, "Magnetohydrodynamic Energy Conversion", pp 23-26, McGraw-Hill, New York, 1968.

[6] H. Griem,"Plasma Spectroscopy", p197, McGraw-Hill, New York, 1964.

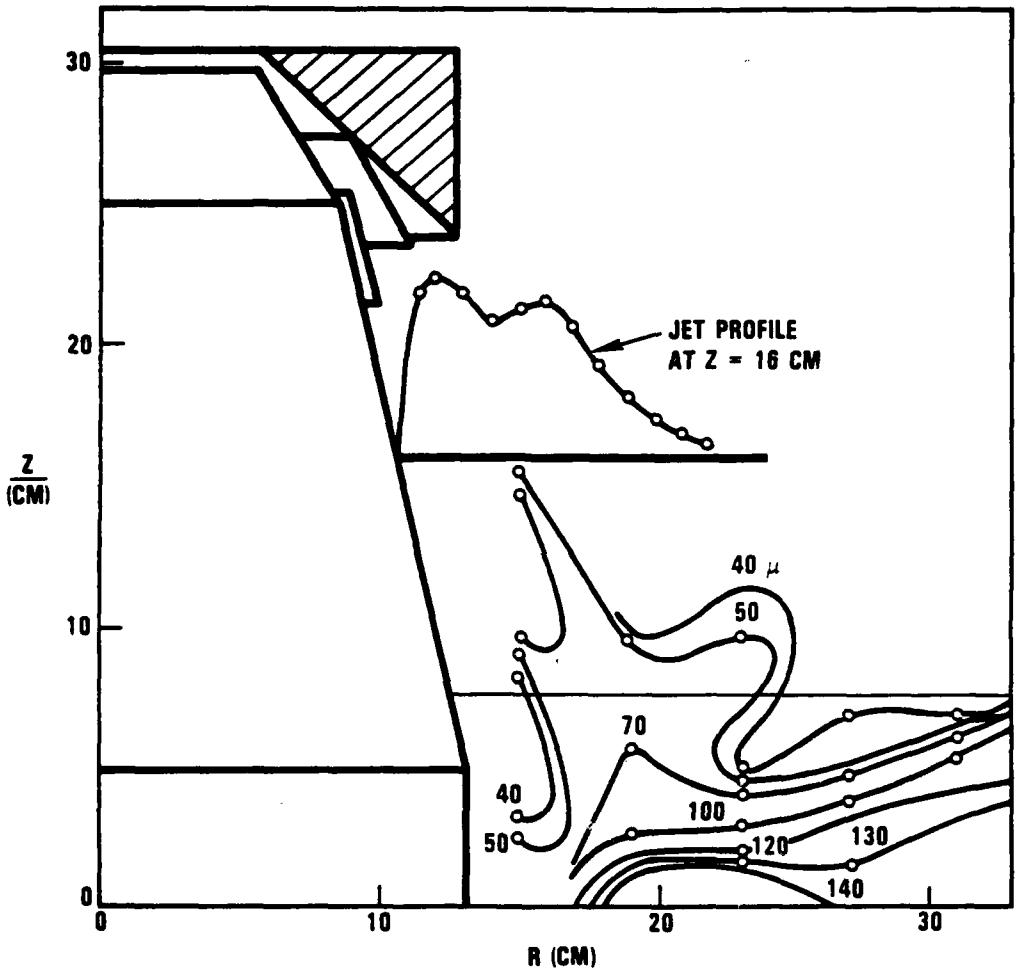

FIGURE 1. ARGON PRESSURE DISTRIBUTION AT 1.2 ms

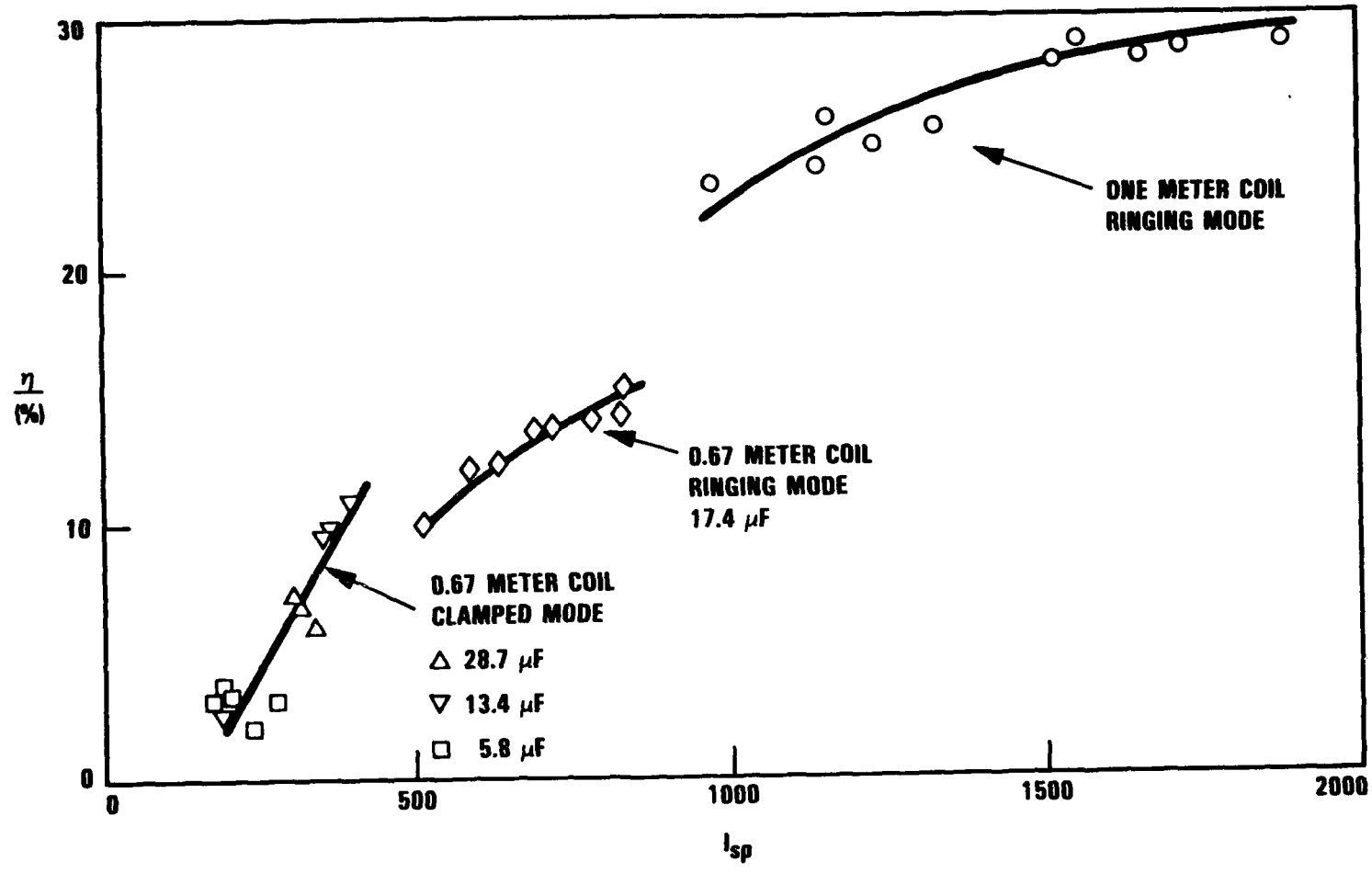

FIGURE 2. THRUSTER EFFICIENCY vs. I_{SP} FOR DIFFERENT THRUSTERS (ARGON)

01.339.88.01 4243

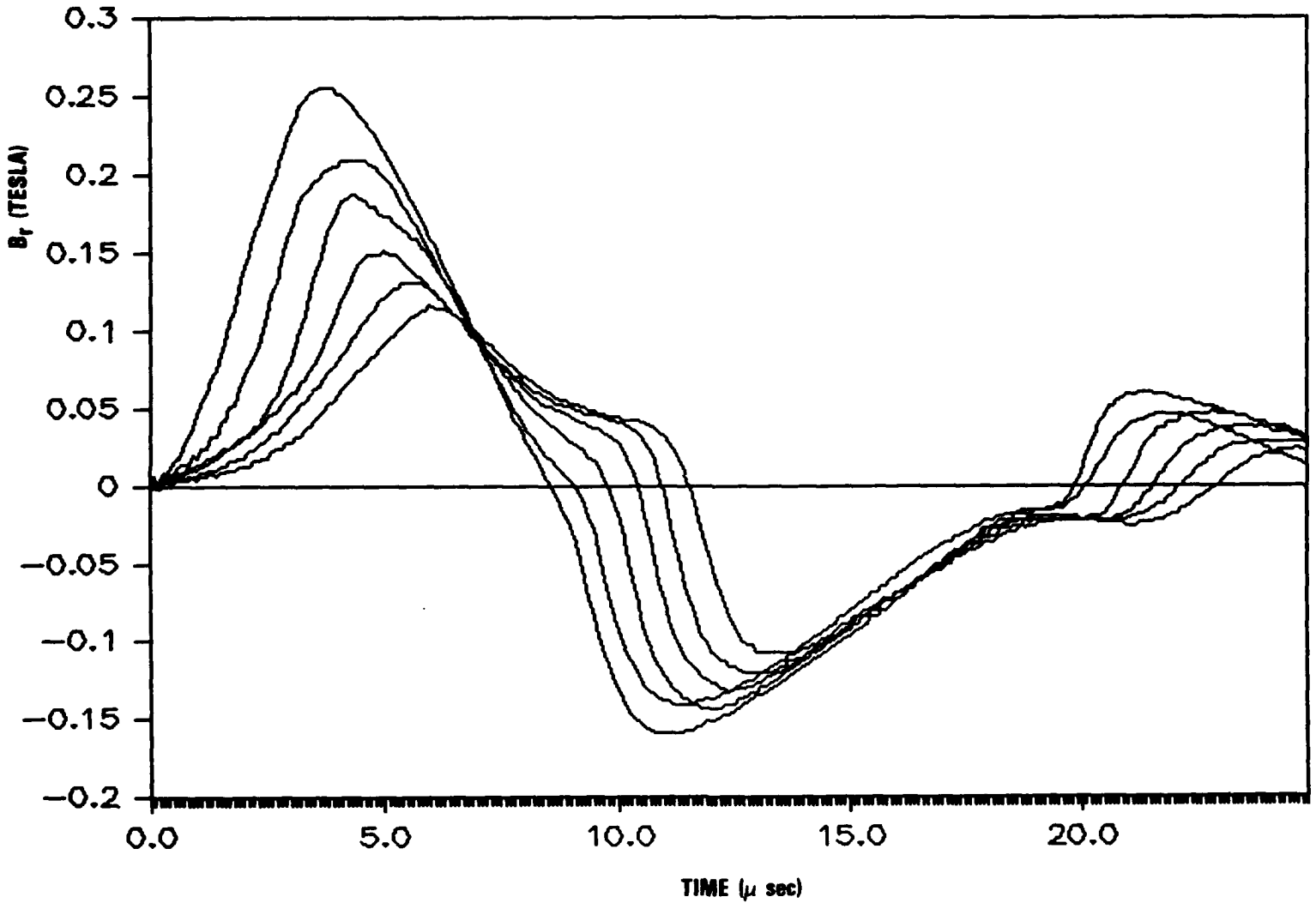

FIGURE 3. MK IV, B_R vs. TIME FOR z = 1, 2, 3, 4, 5, 6 cm

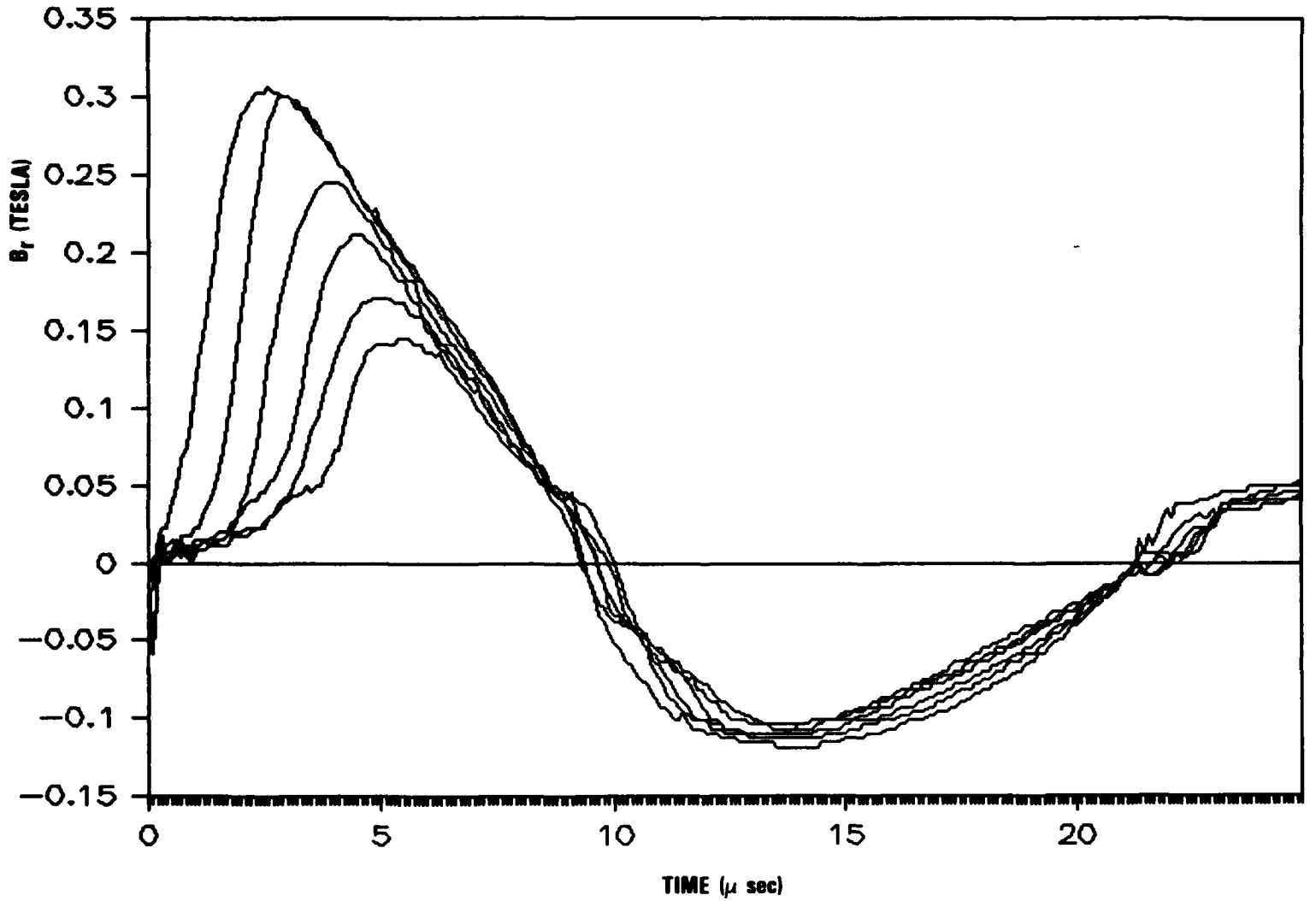

FIGURE 4. MK I, B_R vs. TIME FOR z = 1, 2, 3, 4, 5, 6 CM

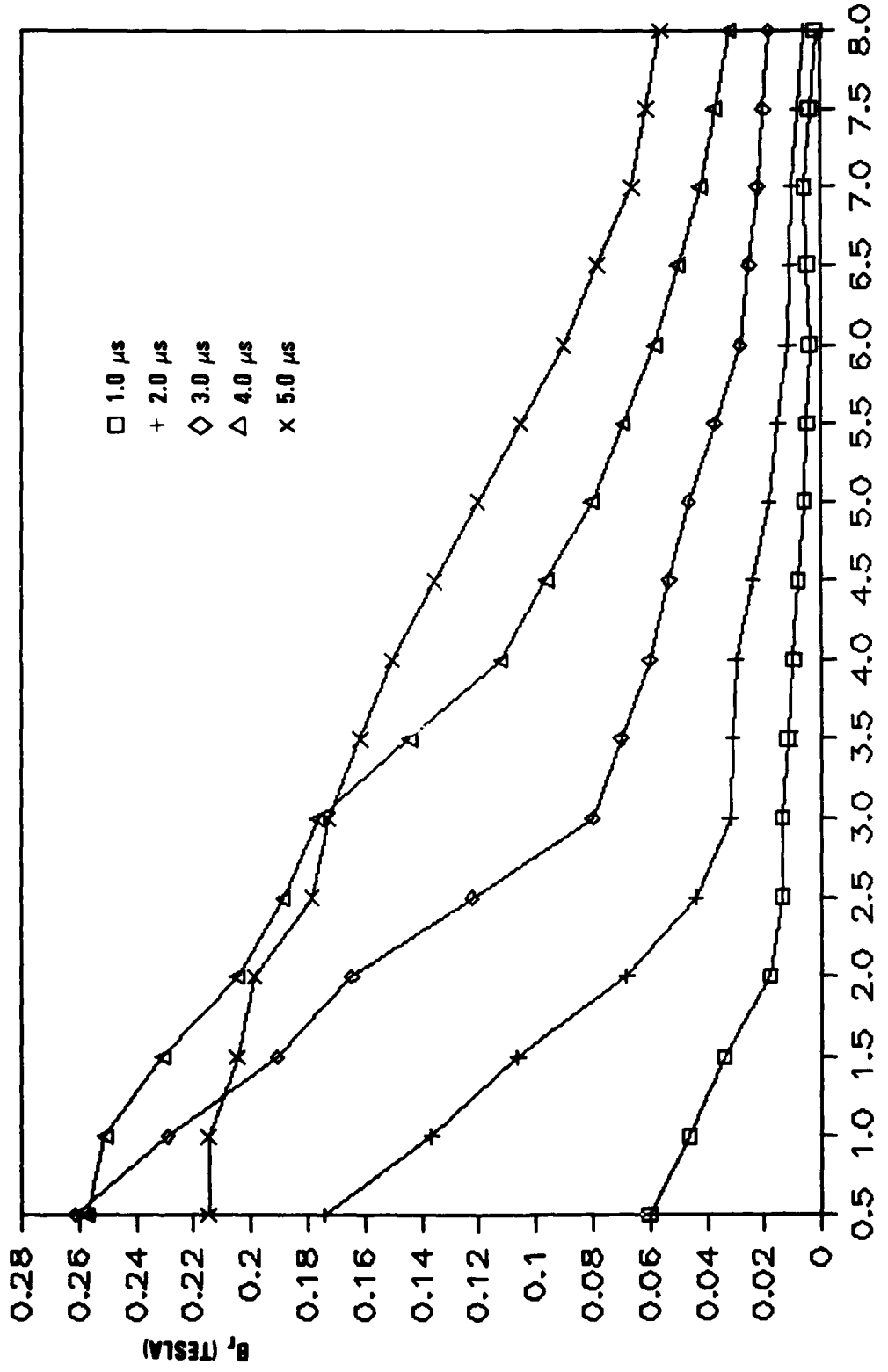

FIGURE 5. MK IV, B_R vs. z AT DIFFERENT TIMES

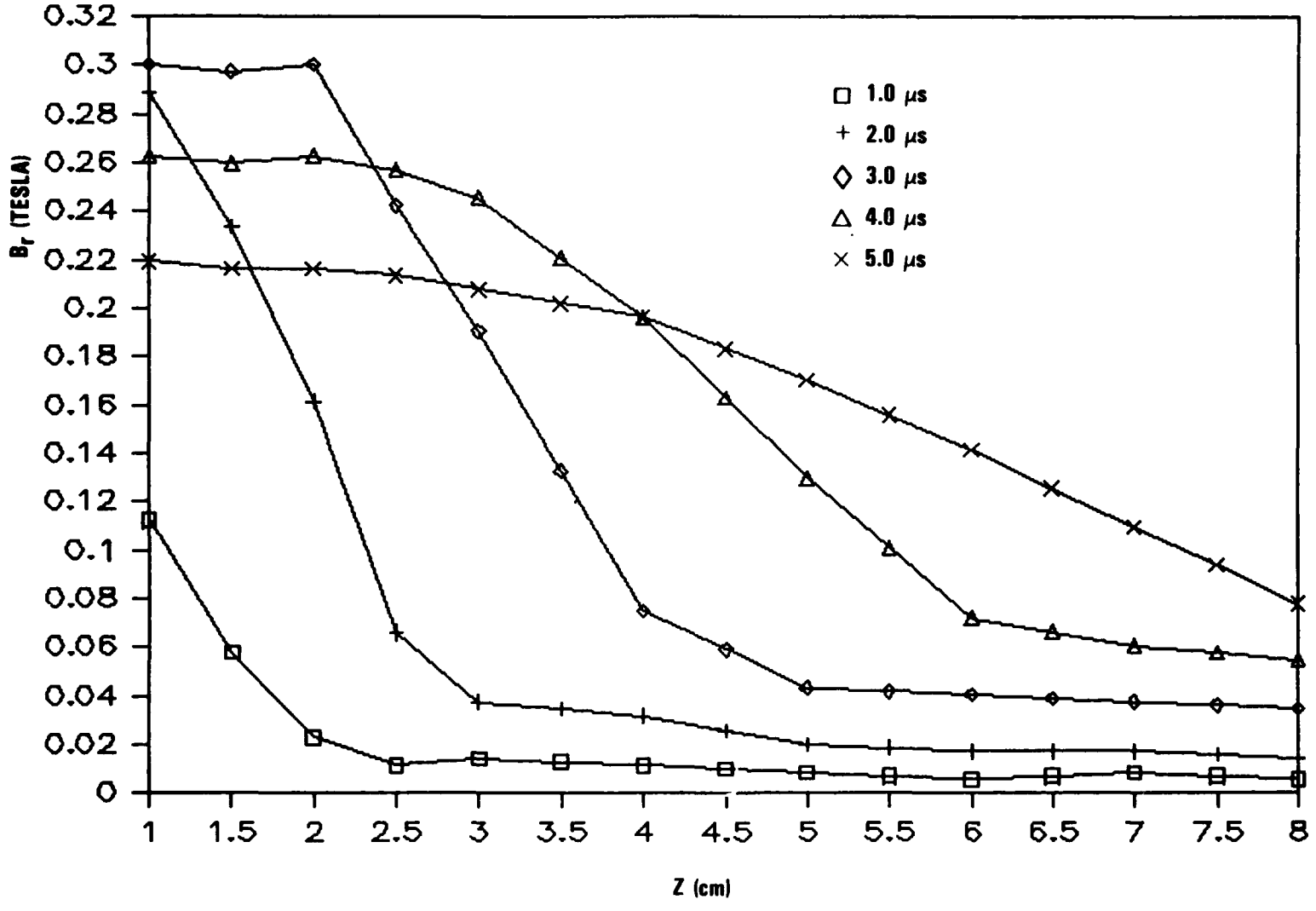

FIGURE 6. MK I, B_R vs. z AT DIFFERENT TIMES

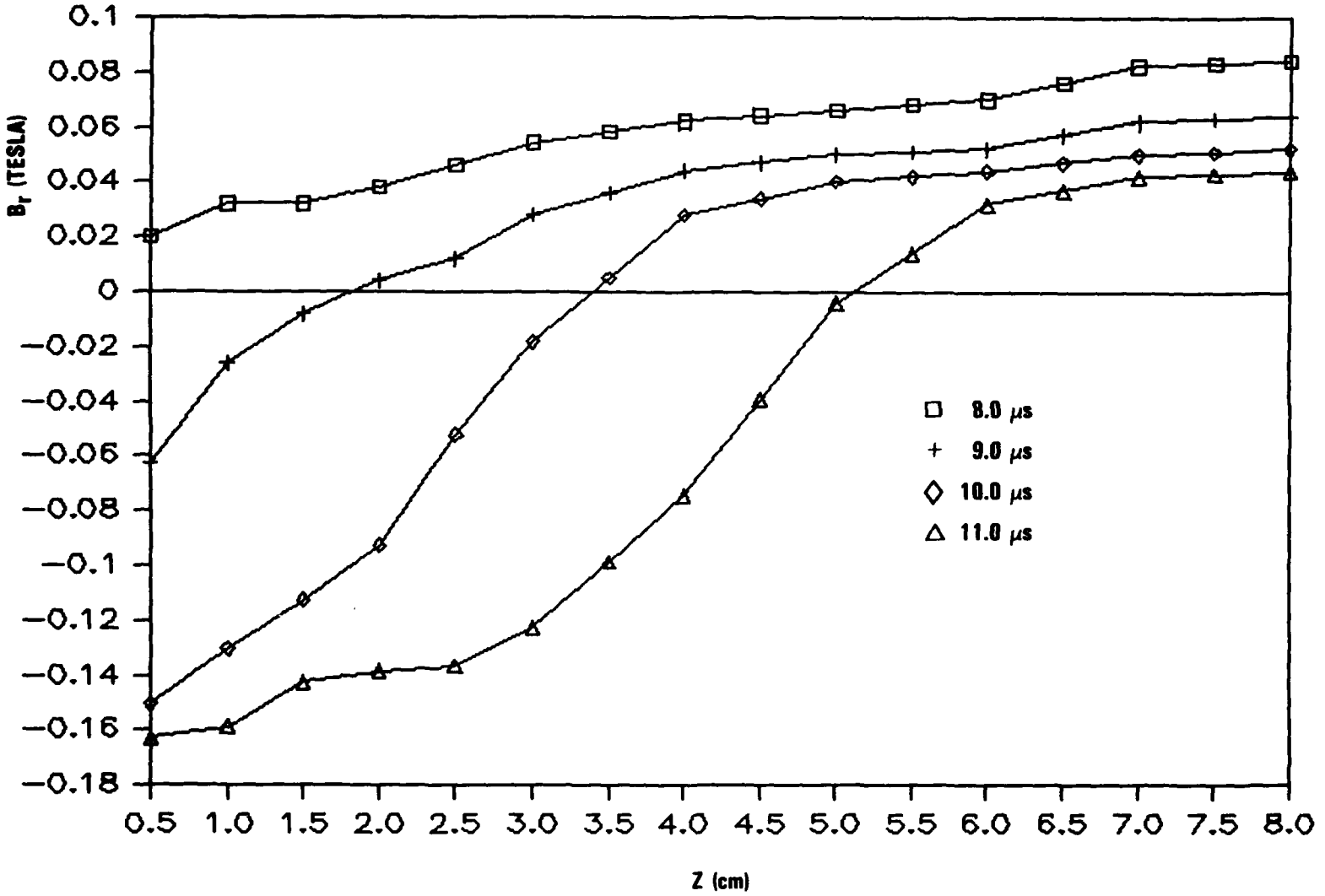

FIGURE 7. MK IV, SECOND HALF-CYCLE, B_R vs. z AT DIFFERENT TIMES

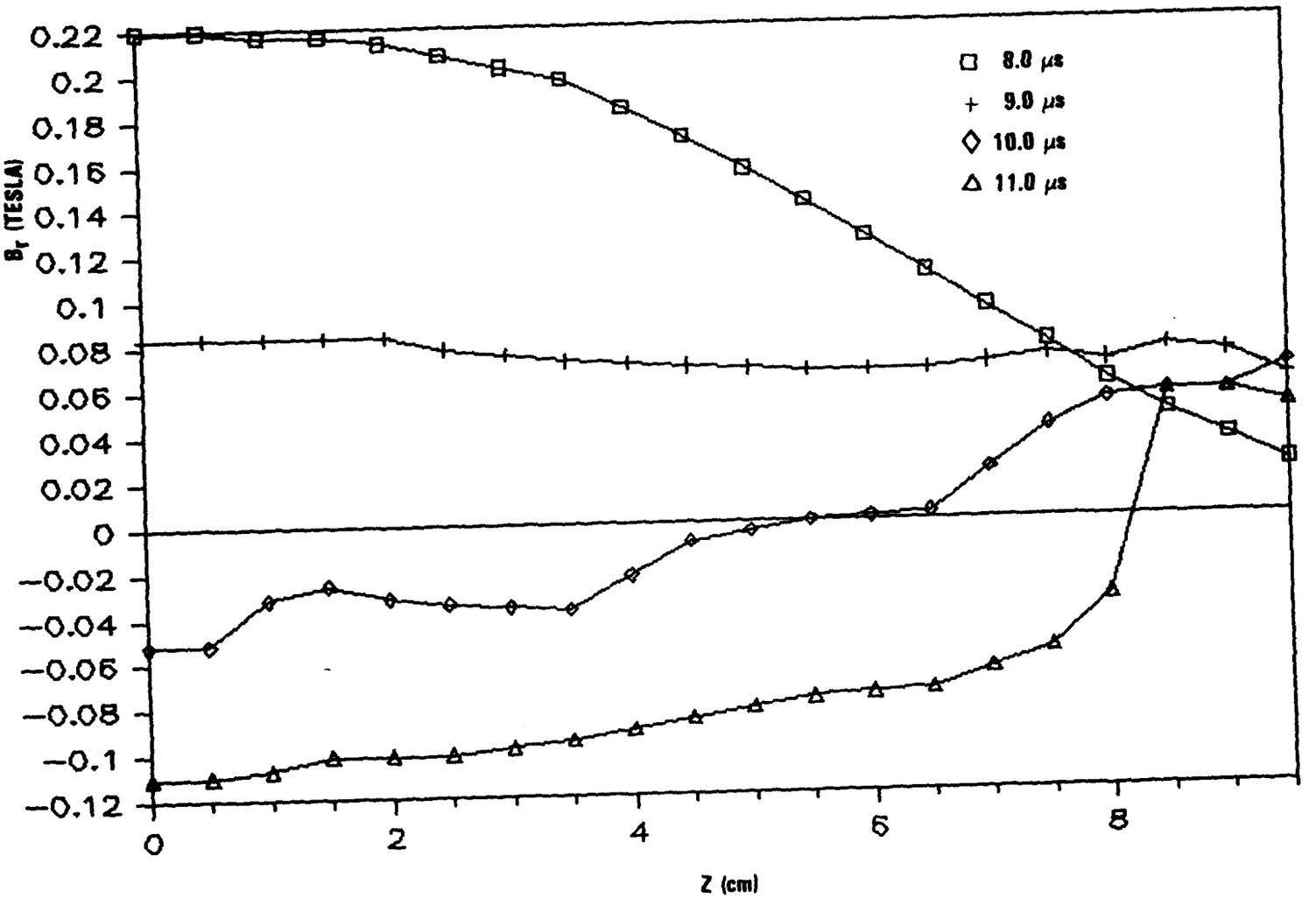

FIGURE 8. MK I, SECOND HALF-CYCLE, B_R vs z AT DIFFERENT TIMES

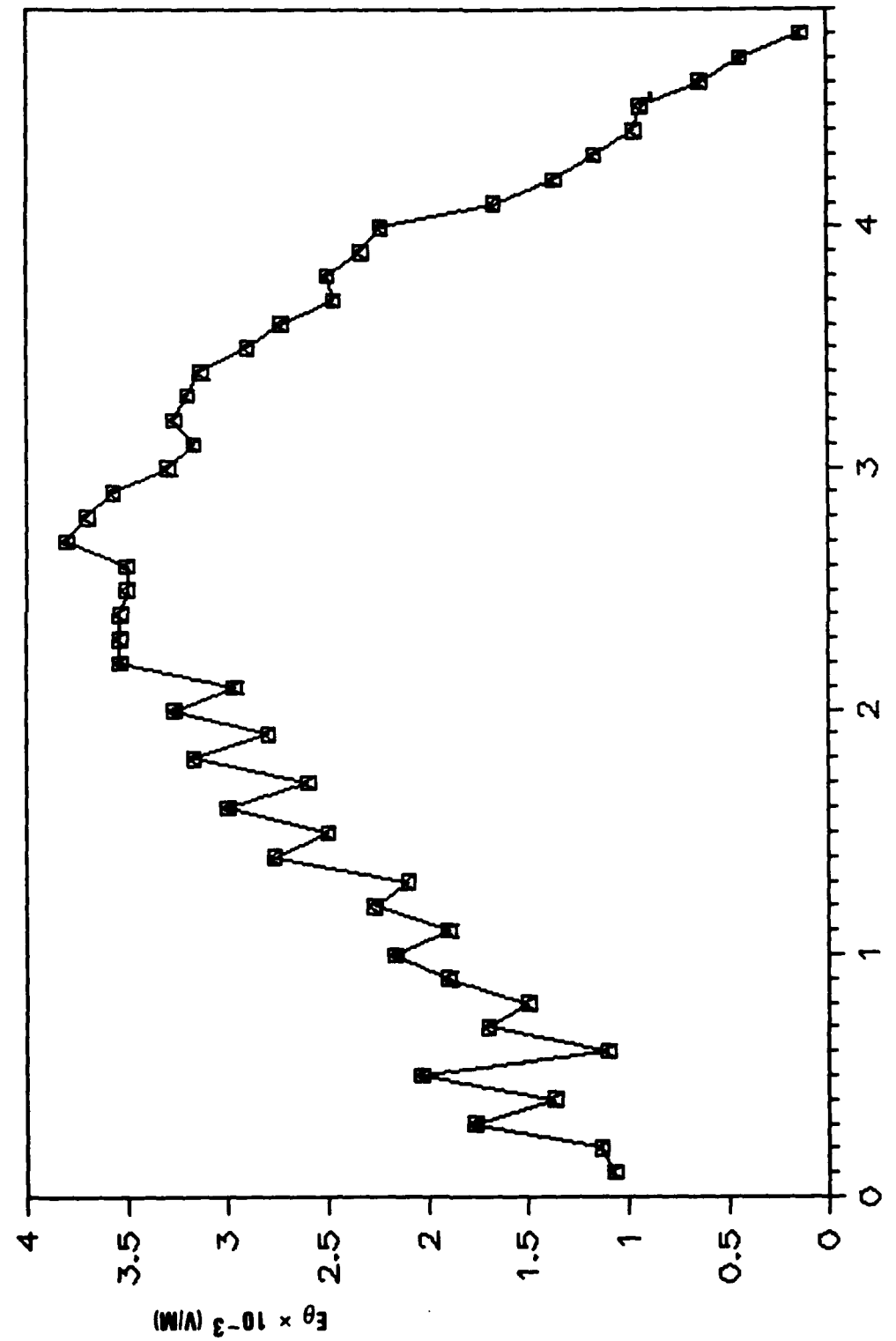

FIGURE 9. MK IV, AZIMUTHAL ELECTRIC FIELD vs. TIME

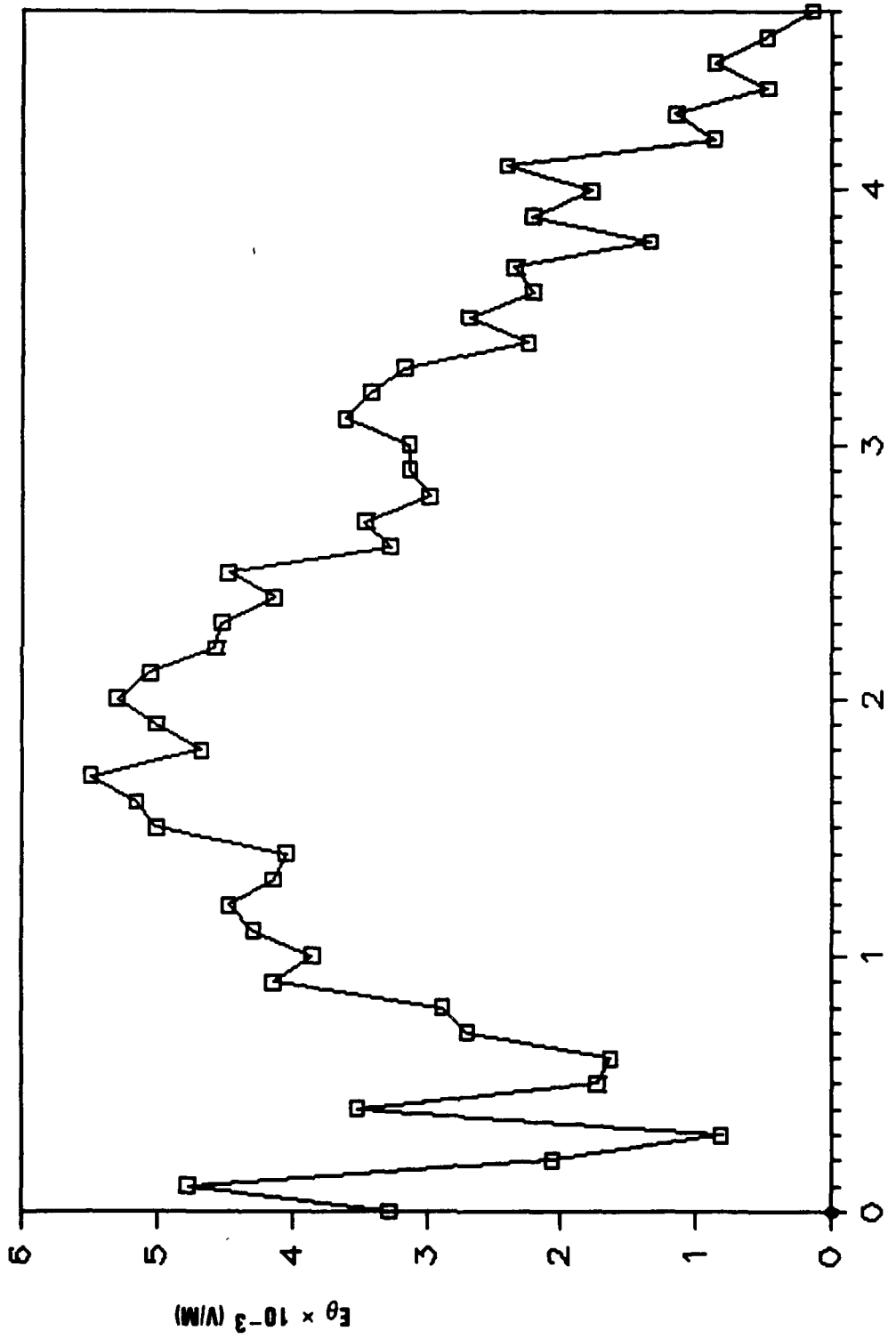

FIGURE 10. MK I, AZIMUTHAL ELECTRIC FIELD vs. TIME

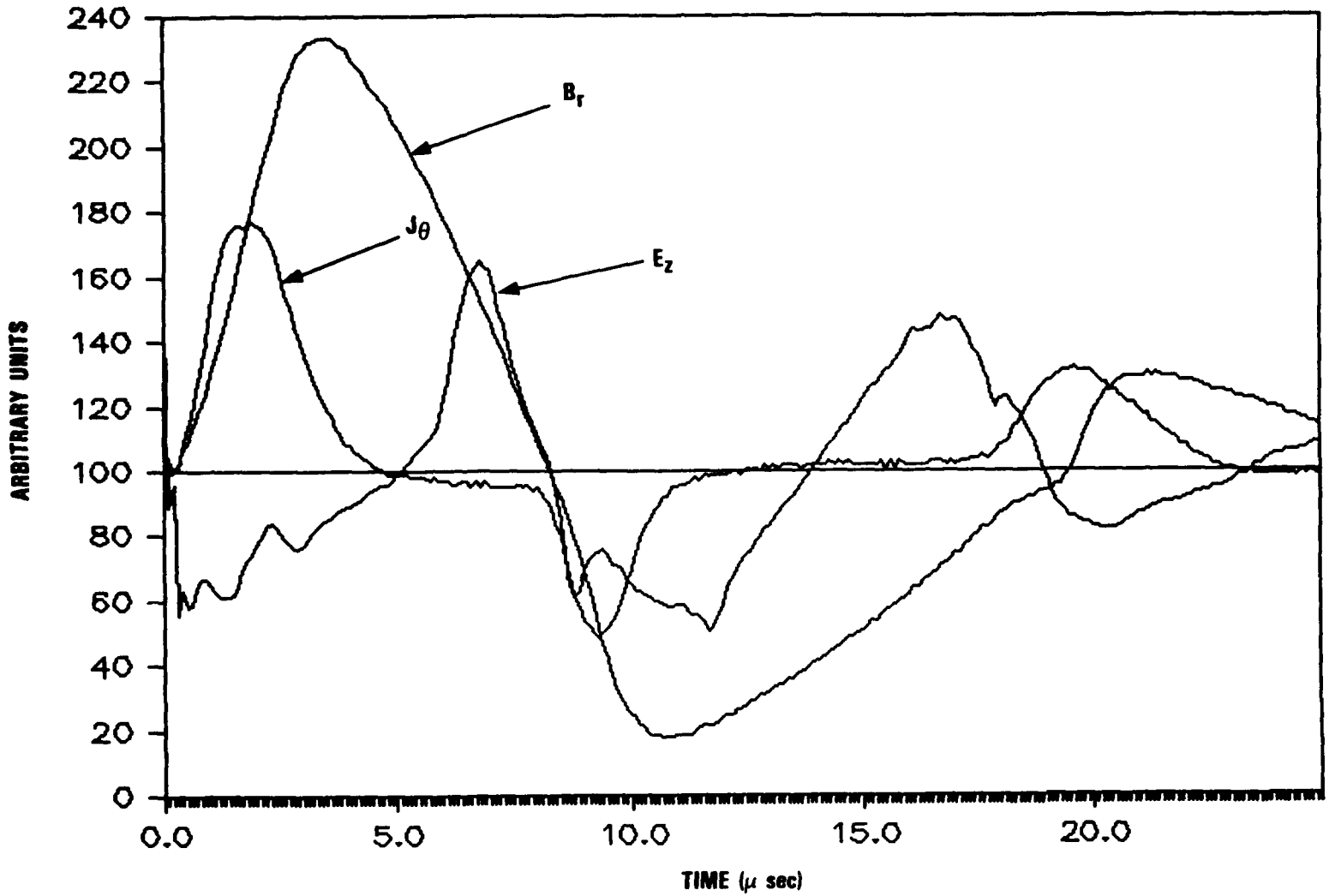

FIGURE 11. MK IV, B_R, E_Z AND J_θ vs. TIME AT z = 0.5 cm

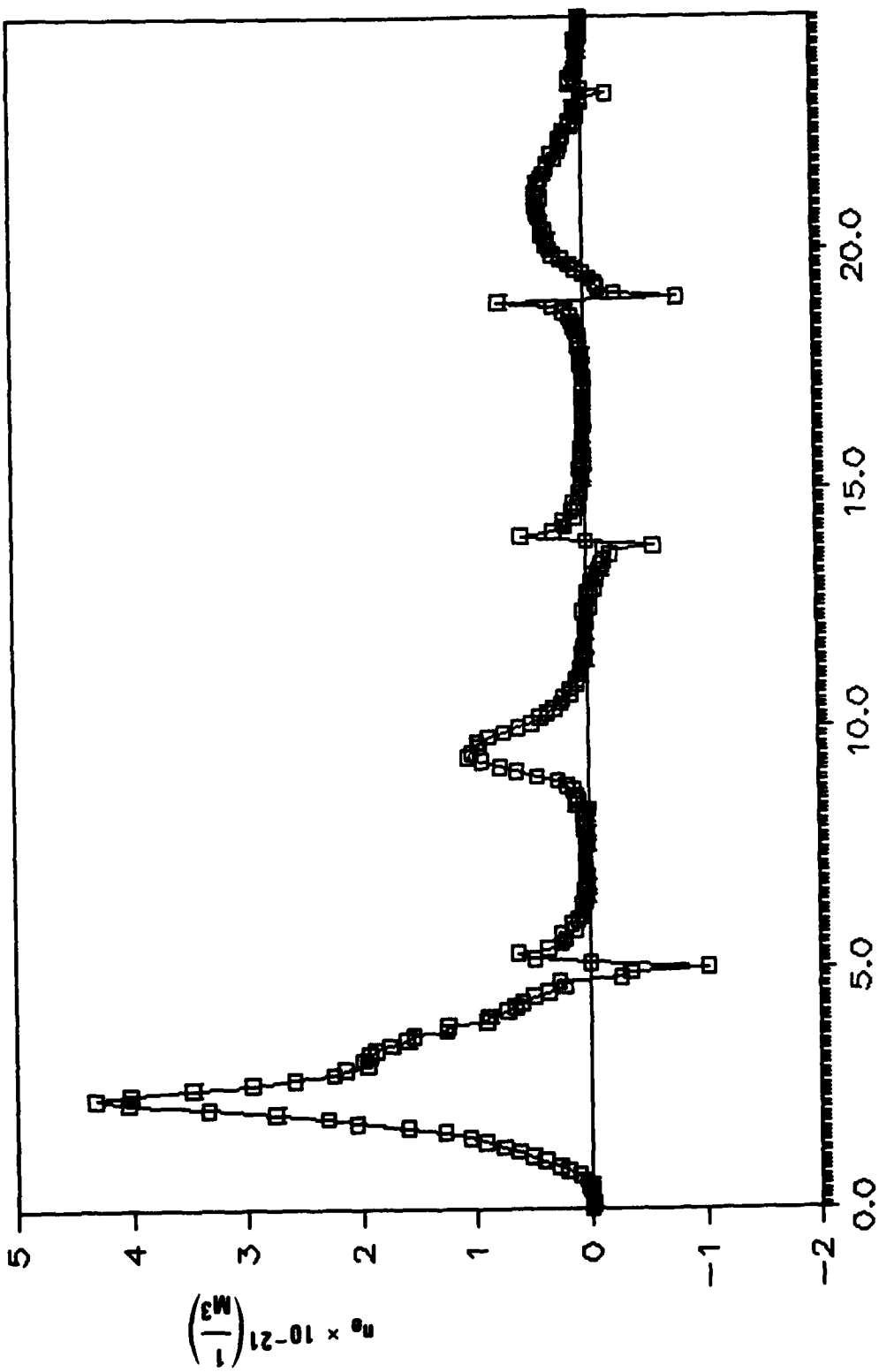

FIGURE 12. MK IV, ELECTRON DENSITY vs. TIME AT z = 0.5 CM

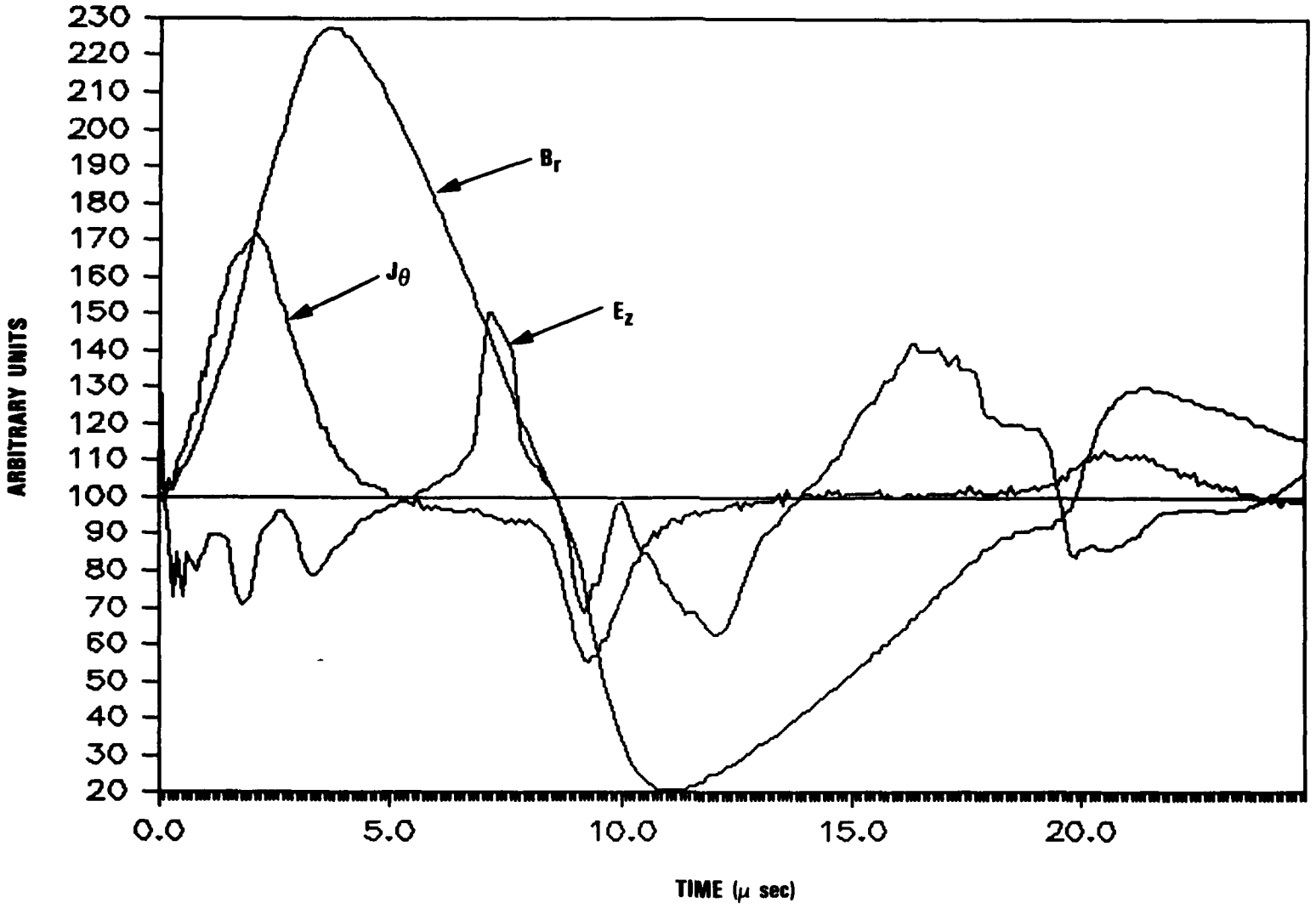

FIGURE 13. MK IV, B_R, E_Z AND J_θ vs. TIME AT z = 1.0 cm

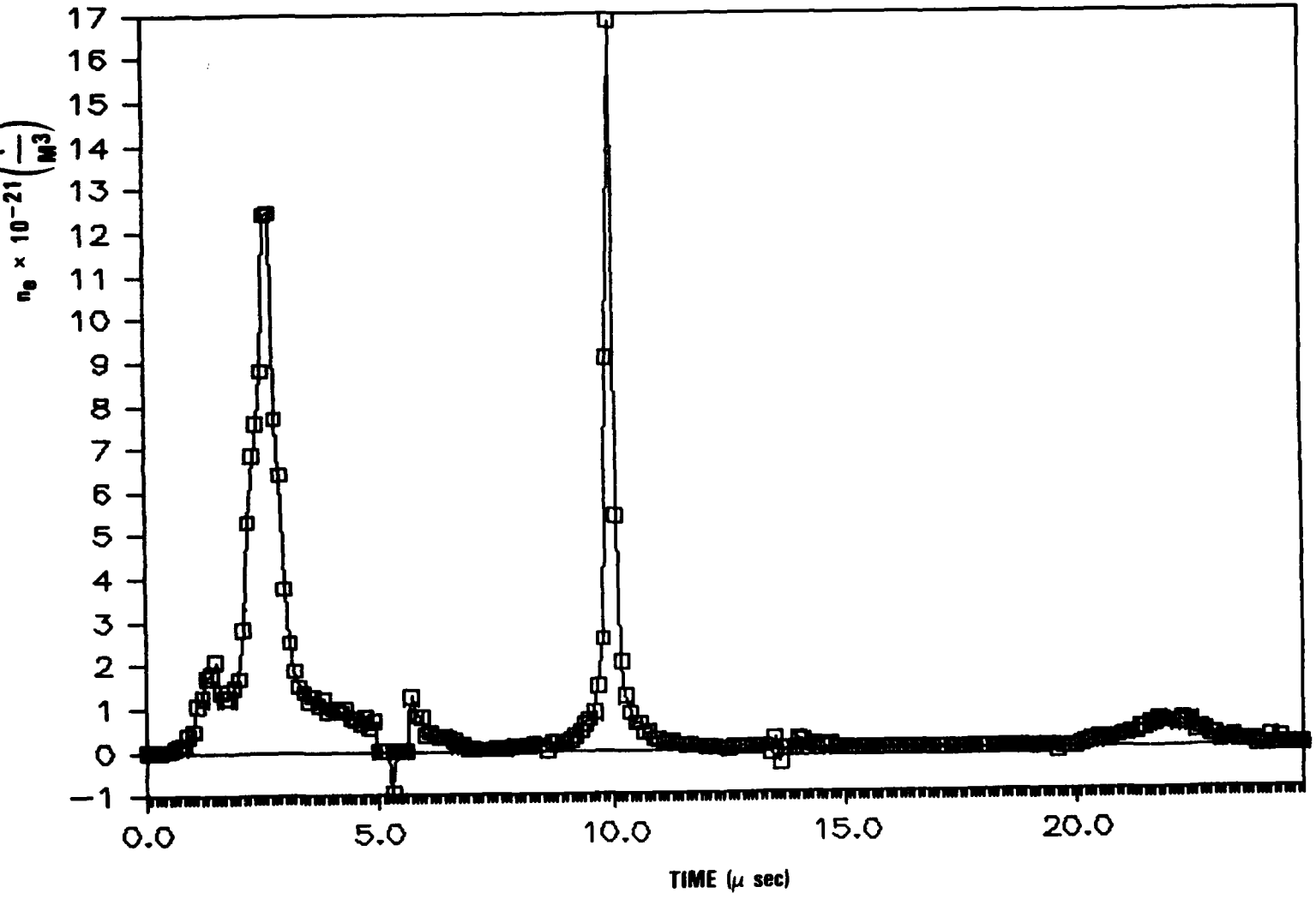

FIGURE 14. MK IV, ELECTRON DENSITY vs. TIME AT z = 1.0 cm

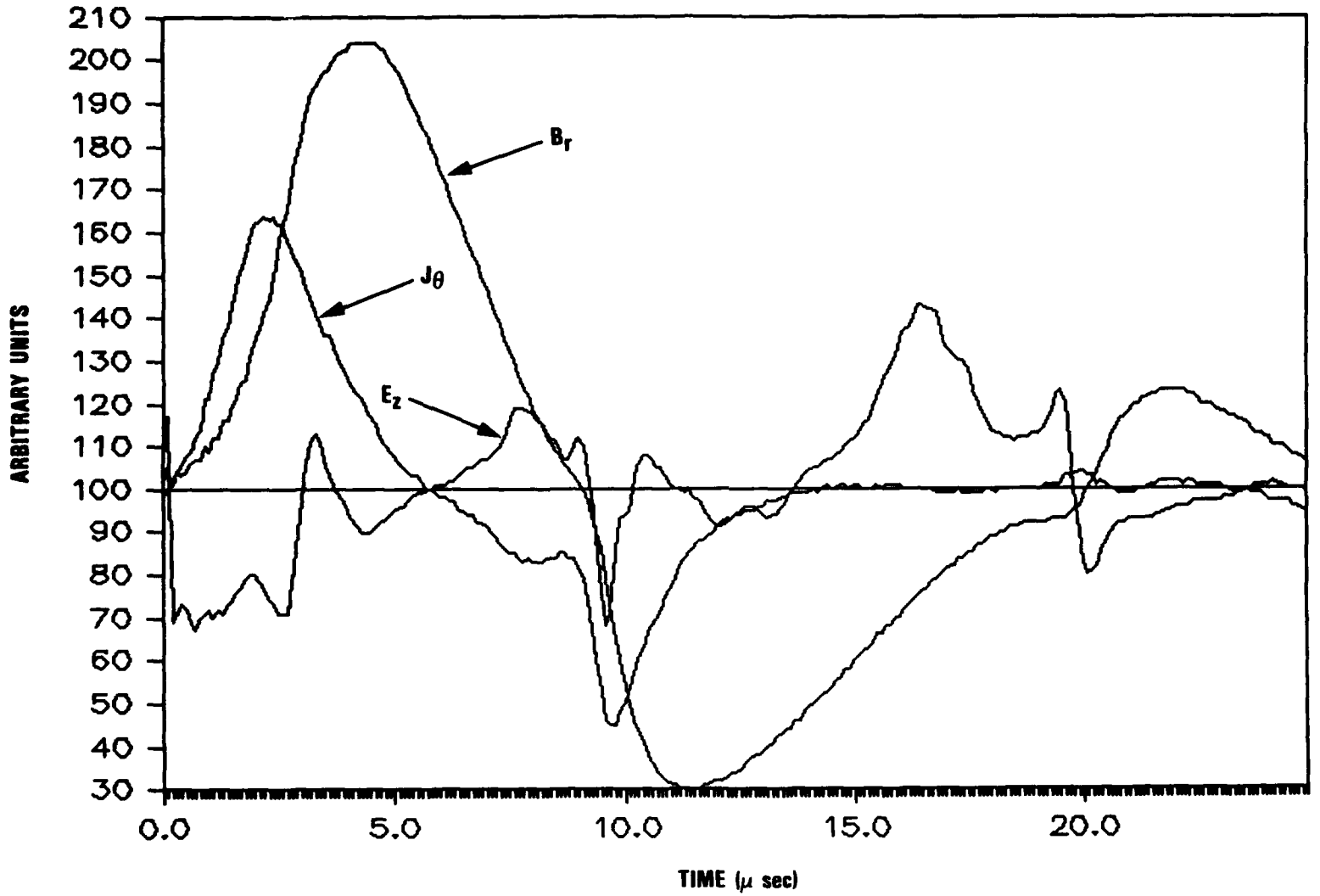

FIGURE 15. MK IV, B_R, E_Z AND J_θ vs. TIME AT z = 2.0 cm

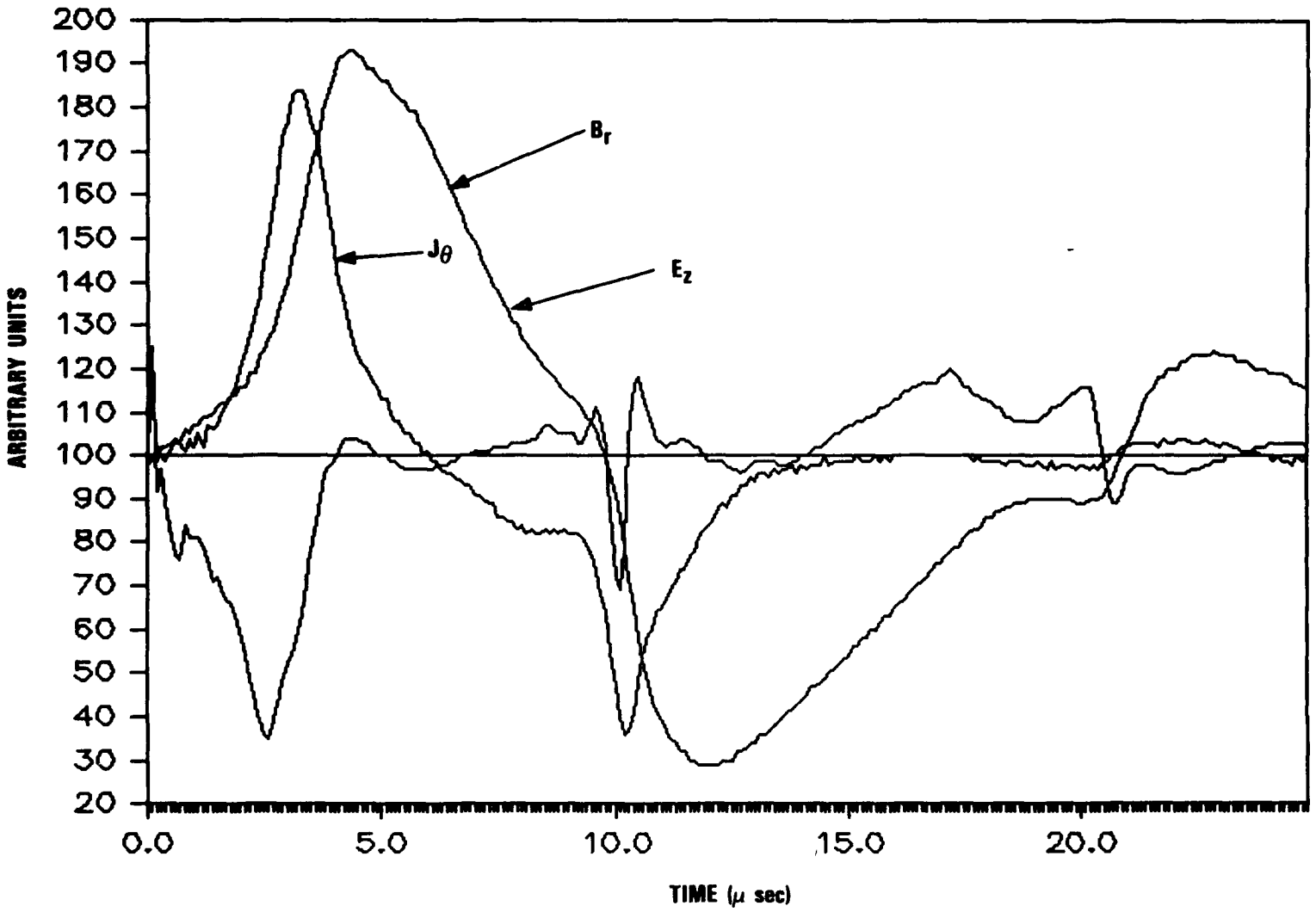

FIGURE 16. MK IV, B_R, E_Z AND J_θ vs. TIME AT z = 3.0 cm

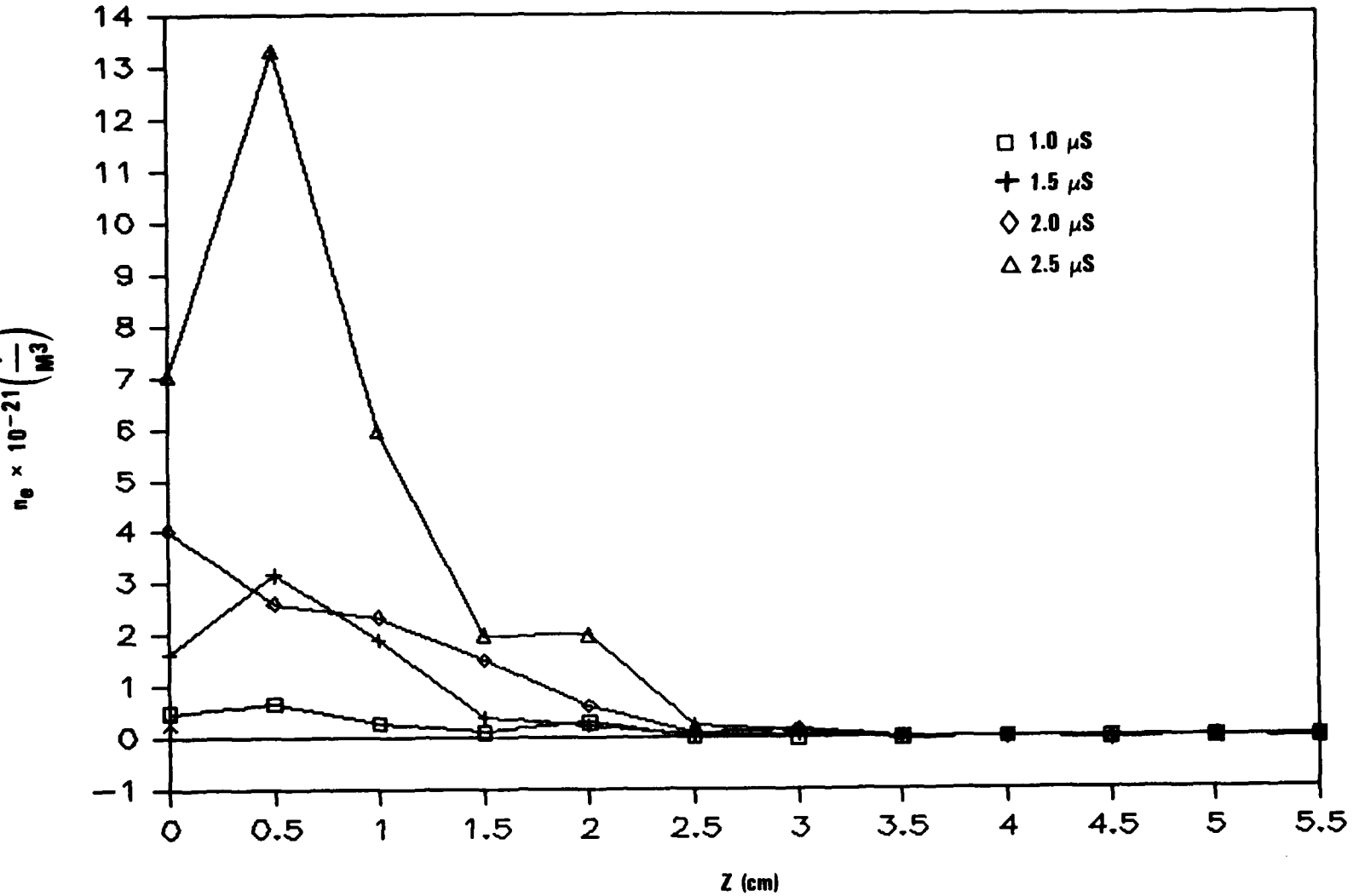

FIGURE 17. MK IV, ELECTRON DENSITY vs. z AT DIFFERENT TIMES

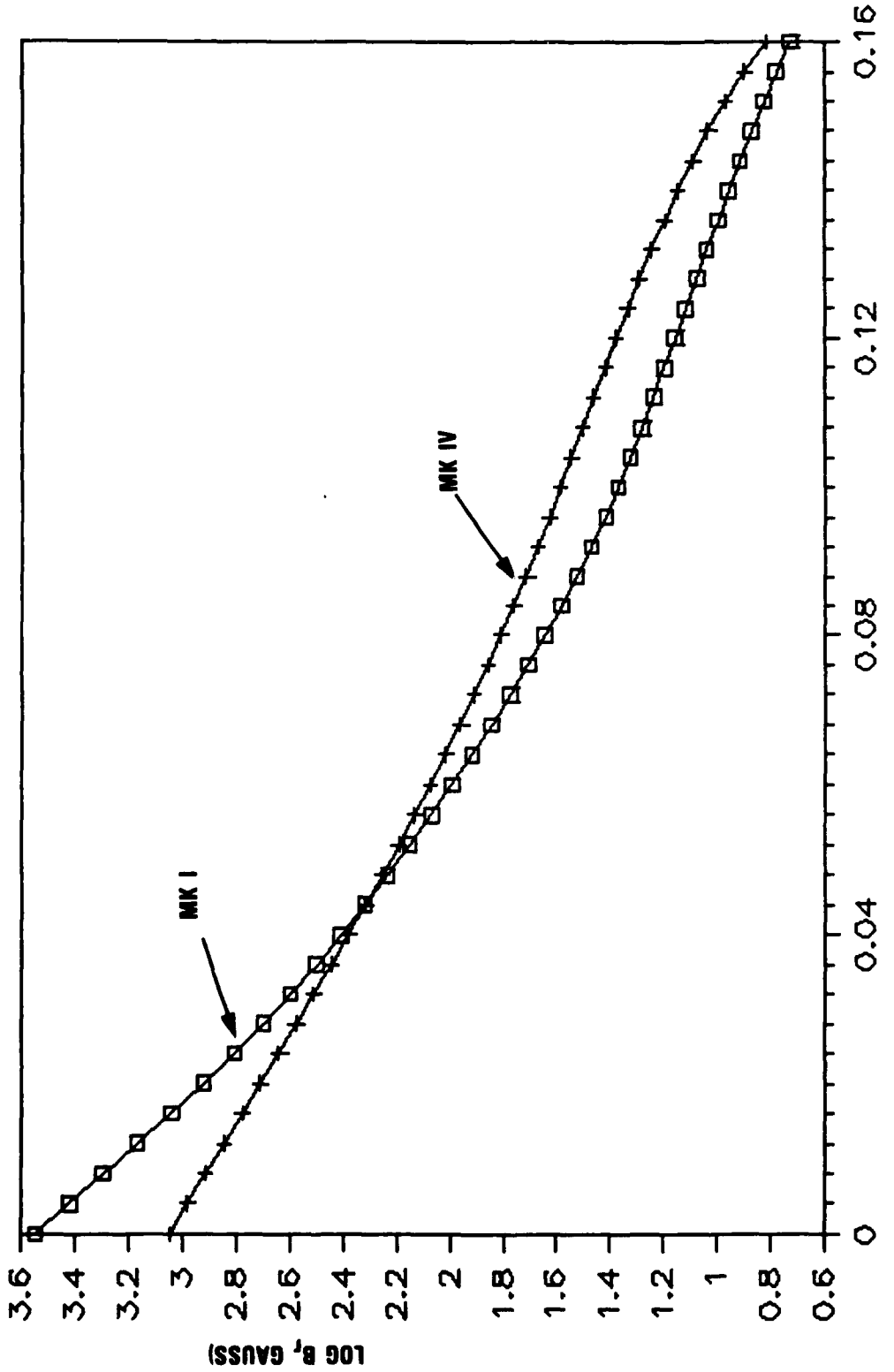

FIGURE 18. LOG B_R VS. Z FOR MK I AND MK IV